

# Oceanic forcing of the Eurasian Ice Sheet on millennial time scales during the Last Glacial Period

Jorge Alvarez-Solas<sup>1,2</sup>, Rubén Banderas<sup>1,2</sup>, Alexander Robinson<sup>1,2,3,4</sup>, and Marisa Montoya<sup>1,2</sup>

<sup>1</sup>Dpto. Astrofísica y Ciencias de la Atmósfera; Facultad de Ciencias Físicas; Universidad Complutense de Madrid (UCM)

<sup>2</sup>Instituto de Geociencias (UCM-CSIC), Madrid, Spain

<sup>3</sup>Potsdam Institute for Climate Impact Research (PIK), Potsdam, Germany

<sup>4</sup>Faculty of Geology and Geoenvironment, National and Kapodistrian University of Athens, Greece

*Correspondence to:* Jorge Alvarez-Solas (jorge.alvarez.solas@fis.ucm.es)

## Abstract.

The last glacial period (LGP; ca.110-10 ka BP) was marked by the existence of two types of abrupt climatic changes, Dansgaard-Oeschger (DO) and Heinrich (H) events. Although the mechanisms behind these are not fully understood, it is generally accepted that the presence of ice sheets played an important role in their occurrence. While an important effort has been made to investigate the dynamics and evolution of the Laurentide Ice Sheet (LIS) during this period, the Eurasian Ice Sheet (EIS) has not received much attention, in particular from a modeling perspective. However, meltwater discharge from this and other ice sheets surrounding the Nordic Seas is often implied as a potential cause of ocean instabilities that lead to glacial abrupt climate changes. Thus, a better understanding of its variations during the LGP is important to understand its role in glacial abrupt climate changes. Here we investigate the response of the EIS to millennial-scale climate variability during the LGP. We use a hybrid, three-dimensional, thermomechanical ice-sheet model that includes ice shelves and ice streams. The model is forced offline through a novel perturbative approach that includes the effect of both atmospheric and oceanic variations and provides a more realistic treatment of millennial-scale climatic variability than conventional methods. **Rev. 1 General Comment (GC) 4:** Our results show that the EIS responds with enhanced ice discharge in phase with interstadial warming in the North Atlantic when forced with surface ocean temperatures. Conversely, when subsurface ocean temperatures are used, enhanced ice discharge occurs both during stadials and at the beginning of the interstadials. Separating the atmospheric and oceanic effects demonstrates the major role of the ocean in controlling the dynamics of the EIS on millennial time scales. **Rev. 1 GC4 and Rev. 2 GC9:** While the atmospheric forcing alone is only able to produce modest iceberg discharges, warming of the ocean leads to higher rates of iceberg discharges as a result of relatively strong basal melting at the margins of the ice sheet. Together with previous work, our results provide a consistent explanation for the response of the LIS and the EIS to glacial abrupt climate changes, and highlight the need for stronger constraints on the local North Atlantic behavior in order to improve our understanding of ice sheet's glacial dynamics.

## 1 Introduction

The last glacial period (LGP; ca.110-10 ka before present, BP) was marked by the existence of two types of abrupt climatic changes: Dansgaard-Oeschger (DO) and Heinrich (H) events (e.g. Alley et al., 1999). DO-events are identified in Greenland ice-core records as regional abrupt warmings by up to 16°C (Huber et al., 2006; Kindler et al., 2014) from cold (stadial) to relatively warm (interstadial) conditions within decades (Dansgaard et al., 1993) followed by a gradual cooling interval lasting from centuries to millennia and an ultimate phase of rapid cooling back to stadial conditions (Steffensen et al., 2008). Superimposed on the millennial-scale variability associated with DO-events, an additional lower-frequency climatic cycle is identified. So-called Bond cycles are flanked by prolonged stadials ending with prominent DO-events within about 7-10 kyr (Bond et al., 1993). Preceding these, and concomitant with the culmination of the prolonged stadials, H-events are registered in North Atlantic marine sediments as layers of remarkably high concentrations of ice-rafted debris (IRD) (Heinrich, 1988) as a result of massive iceberg discharges from the Laurentide ice-sheet (LIS) (Hemming, 2004).

While significant effort has been invested in understanding the role of the LIS in glacial abrupt climate changes, the dynamics of the Eurasian Ice Sheet (EIS) during the LGP has received comparatively less attention from a modeling perspective. However, improving our understanding of its evolution and response to past climate changes is important for a number of reasons. First, constraining freshwater inputs into the North Atlantic Ocean is crucial for a better understanding of the driving mechanisms of glacial abrupt climate changes (Rasmussen and Thomsen, 2013), since meltwater discharge from the ice sheets surrounding the Nordic Seas is often implied as a cause of ocean instabilities. Precursor events could possibly have originated from the European and Icelandic ice sheets (Grousset et al., 2000; Scourse et al., 2000). Meltwater peaks in the Norwegian Sea during Marine Isotopic Stage 3 (MIS 3) have been associated with H events and millennial-scale climate variability (Lekens et al., 2006). From a broader perspective, the EIS, consisting of the Fennoscandian, the British Isles and the Barents-Kara ice sheets (FIS, BIIS and BKSIS, respectively) contained a large marine-based sector at its maximum extension (Hughes et al., 2016) that was exposed to oceanic variations, and the BKSIS is often considered as an analog for the current West Antarctic ice sheet (WAIS). At the LGM both had a similar size, but while the WAIS endured the deglaciation, the BKSIS completely disappeared (Andreassen and Winsborrow, 2009). Understanding the underlying mechanisms would provide important insights into the future evolution of the WAIS (Gudlaugsson et al., 2013, 2017).

Reconstructing the EIS response to past glacial abrupt climate changes prior to the LGM has been difficult, in part because, in reaching its maximum extent, the ice sheet eroded and removed nearly all older deposits. Nevertheless, the available paleodata indicate that during MIS 3 the EIS was highly dynamic, with its advance and retreat closely linked to stadials and interstadials. In this line, records from Norway (Mangerud et al., 2003, 2010; Olsen et al., 2002), Finland (Helmens and Engels, 2010) and Sweden (Wohlfarth, 2010) indicate rapid and rhythmic ice-sheet variations in western Scandinavia, with advances and retreats during stadials and interstadials, respectively. Recent records also indicate enhanced meltwater discharges during interstadials from the Svalbard-Barents Sea ice sheet and probably also from the Scandinavian ice sheet (Rasmussen and Thomsen, 2013). The resolution and quality of geophysical data across marine sectors has improved considerably in the past decade (Hughes et al. (2016) and references therein). The results confirm substantial variations of the EIS volume, with the largest uncertainties

in marine sectors of the ice sheets. Strong variations in the deposition of IRD suggests high co-variability of the BIIS with changes in ocean sea surface temperature (Hall et al., 2011; Scourse et al., 2009) and variations in EIS ice streams (Becker et al., 2017). North Atlantic marine sediment records register widespread variations of IRD input throughout the LGP indicating variations of iceberg rafting from virtually all surrounding ice sheets. Sources and timing differ among different sites. A dominant periodicity equal to that of DO-events was identified in the Irminger Sea, with the largest IRD peaks at the end of stadials originating in the Iceland and Greenland ice sheets (von Kreveld et al., 2000). Strong millennial-scale iceberg rafting variability of the BIIS has been documented as well in the North Sea (Hall et al., 2011; Peck et al., 2007; Scourse et al., 2009), but enhanced IRD seems to occur both during interstadials and stadials. For the FIS, IRD records in the Norwegian Sea show the characteristic DO periodicity, with IRD discharge occurring just before interstadial transitions (Lekens et al., 2006). More recently, however, an increase in IRDs from Fennoscandia during interstadials has been reported (Dokken et al., 2013; Becker et al., 2017). **Rev. 1 Specific comment (SC) 1: Correlating IRD occurrence with temperature changes registered in Greenland remains difficult, however, because it requires an extremely well dated chronology to assess the phasing between ocean sediments and ice cores.**

Progress has been achieved also in the past decade using ice-sheet models. Siegert and Dowdeswell (2004) used inverse modelling to simulate the EIS evolution during the second part of the LGP, matching the geological evidence presented by optimizing the fit with data. Forsström and Greve (2004) used subsequent versions of a three-dimensional, polythermal ice-sheet model to simulate the EIS evolution throughout the LGP. Important variations in the EIS ice volume in response to temperature and precipitation variations were simulated. Clason et al. (2014) additionally included a parameterisation of surface meltwater enhanced sliding. In both cases too much ice was simulated in the northeastern EIS. Gudlaugsson et al. (2017) used the same model but introducing a simple representation of the subglacial hydrological system, focusing on its role in the temporal evolution of the EIS. Recently, an ice-sheet model constrained by data has been used to simulate the EIS evolution throughout part of LGP (Patton et al., 2016). The model targets the most probable EIS distribution at different time slices and reproduces substantial ice-volume variations. However, all of these models suffer from limitations, such as the use of the shallow-ice approximation (SIA) and its associated lack of an explicit treatment of the oceanic forcing. Marshall and Koutnik (2006) investigated the production of icebergs from all the North American ice sheets with a parameterized calving model. They found different behaviors on millennial time-scales depending on the local glaciological and climatic characteristic, with increased iceberg production both during stadials (e.g. from Iceland) or during interstadials (e.g. from Barents Sea). Nonetheless, sub-marine melting at the grounding line has not been explicitly considered until now and its impacts on millennial-scale variability have not been investigated up to now from a modelling perspective.

Here, we investigate the response of the EIS to millennial-scale climate variability during MIS 3 using a three-dimensional ice-sheet model. To this end, a novel offline approach is used that provides a better representation of millennial-scale climate variability (Banderas et al., 2017). In addition, for the first time, both the atmospheric and oceanic effects of millennial scale climate variability associated with glacial abrupt climate changes are considered. This facilitates the quantification of the relative contribution of surface (ablation) and dynamic processes related to ice-ocean interactions.

The paper is organized as follows: in Section 2 the ice-sheet model, the forcing method and the experimental setup are described. In Section 3 the response of the EIS to the imposed forcing is shown, the focus being the evolution of its ice volume, its impact on sea level and the mechanisms behind meltwater and ice discharge. Finally, the main conclusions are summarised in Section 5.

## 5 2 Model and experimental setup

### 2.1 Model

The model used in this study is the ice-sheet model GRISLI-UCM, an extension of the original model GRISLI developed by Ritz et al. (2001). GRISLI-UCM is a hybrid three-dimensional thermomechanical ice-sheet model. Inland ice flows through deformation under the Shallow Ice Approximation (SIA, Hutter, 1983). Ice shelves and ice streams are described following the Shallow Shelf Approximation (SSA, MacAyeal, 1989). Ice streams (areas of fast flow, typically faster than  $10^2 \text{ m a}^{-1}$ ) are considered as dragging ice shelves, allowing for basal movement of the ice (Bueler and Brown, 2009). Basal stress under ice streams is proportional to ice velocity and to the effective pressure of ice. **Rev. 2 GC7 and SC3:** The effects of varying this proportionality factor on the simulated ice streams are discussed in Alvarez-Solas et al. (2011). The locations of the ice streams are determined by the presence of basal water within areas where the sediment layer is saturated. **Rev. 2 GC7 and SC4:** The criterion to activate SSA inland relies on the presence of water above 1 meter in places of soft sediments (Laske, 1997) and above 400 meters in absence of such sediments. **Rev. 2 GC6, SC5 and SC6:** The grounding line position dynamically evolves following the flotation criterion after the mass conservation equation is solved. Ice on the ice-shelf front calves following a two criteria. First, its thickness must first fall below a threshold ( $H_{calv} = 150 \text{ m}$ , in the standard setup; see the Supplementary Information for further information regarding the dependence of our results on this parameter). Second, the upstream advection must fail to maintain the ice thickness above this threshold following a semi-Lagrangian approach (Peyaud et al., 2007). GRISLI-UCM thus explicitly calculates grounding line migration, ice-stream and ice-shelf velocities. This allows the model to properly represent both grounded and floating ice. GRISLI-UCM uses finite differences on a staggered Cartesian grid at a 40 km resolution, corresponding to  $224 \times 208$  grid points for the Northern Hemisphere domain, including the EIS, with 21 vertical levels. By default, initial topographic conditions are provided by surface and bedrock elevations built from the ETOPO1 dataset (Amante and Eakins, 2009) and ice thickness (Bamber et al., 2001). The surface mass balance is given by the sum of accumulation and ablation, both of which are calculated from monthly surface air temperatures (SATs) and monthly total precipitation. Accumulation is calculated by assuming that the fraction of solid precipitation is proportional to the fraction of the year with mean daily temperature below  $2^\circ\text{C}$ . The daily temperature is computed from monthly SATs assuming that the annual temperature cycle follows a cosine function. Ablation is calculated using the positive-degree-day (PDD) method (Reeh, 1989). **Rev. 2 GC5 and SC7 :** Its main parameters are the standard deviation of daily temperature,  $\sigma$ , and the conversion factors from PDDs to melt for snow and ice,  $f_{\text{PDD}_{\text{snow}}}$  and  $f_{\text{PDD}_{\text{ice}}}$ . Here,  $\sigma = 5 \text{ K}$ ,  $f_{\text{PDD}_{\text{snow}}} = 0.003 \text{ mwe PDD}^{-1}$  and  $f_{\text{PDD}_{\text{ice}}} = 0.008 \text{ mwe PDD}^{-1}$ . Refreezing is considered, with a value of  $C_{\text{si}} = 60\%$ . GRISLI-UCM accounts for changes in elevation at each time step considering a linear atmospheric vertical profile for temperature with different lapse rates in summer and in the

annual mean (0.0080 and 0.0065 K m<sup>-1</sup>, respectively) to account for the smaller summer atmospheric vertical stability (see also the Supplementary Information).

Basal melting inland depends on pressure and water content at the base of the ice sheet **Rev. 2 SC 8** (Ritz et al., 2001) as well as on the geothermal heat flux, which is prescribed from **Rev. 2 SC 9** the reconstruction by Shapiro and Ritzwoller (2004).

- 5 Basal melting for floating ice is computed using a linear temperature anomaly with respect to the freezing point. The details of the implementation of the boundary conditions (SMB and oceanic basal melting) in this particular study are given below (Section 2.2).

## 2.2 Offline forcing method

- SMB and oceanic basal melting are obtained through a time-varying synthetic climatology built through a novel method that is found to provide a more realistic offline forcing for ice-sheet models than classical offline methods (Banderas et al., 2017). The method follows a perturbative approach in the sense that the forcing combines the present-day climatology, obtained from observational data, together with simulated anomalies. But in contrast to usual offline forcing methods, orbital and millennial scale variabilities are not lumped in a sole anomaly pattern but differentiated. The method thus combines present-day observations, simulated Last Glacial Maximum (LGM) anomalies relative to present, scaled by an orbital-timescale index, and simulated stadial-interstadial anomalies, scaled by a millennial-timescale index:

$$\mathbf{T}^{\text{atm}}(t) = \mathbf{T}_0^{\text{atm}} + (1 - \alpha^*(t)) \Delta \mathbf{T}_{\text{orb}}^{\text{atm}} + \beta^*(t) \Delta \mathbf{T}_{\text{mil}}^{\text{atm}} \quad (1)$$

$$\mathbf{P}(t) = \mathbf{P}_0 \{ \alpha^*(t) + (1 - \alpha^*(t)) \delta \mathbf{P}_{\text{orb}} [(1 - \beta^*(t)) + \beta^*(t) \delta \mathbf{P}_{\text{mil}}] \} \quad (2)$$

- Here,  $\mathbf{T}^{\text{atm}}(t)$  and  $\mathbf{P}(t)$  are the SAT and precipitation fields at time  $t$ .  $\mathbf{T}_0^{\text{atm}}$  and  $\mathbf{P}_0$  are the ERA-INTERIM present-day SAT and precipitation climatologies (Dee et al., 2011).  $\Delta \mathbf{T}_{\text{orb}}^{\text{atm}} = \mathbf{T}_{\text{lgm}}^{\text{atm}} - \mathbf{T}_{\text{pd}}^{\text{atm}}$  and  $\delta \mathbf{P}_{\text{orb}} = \mathbf{P}_{\text{lgm}} / \mathbf{P}_{\text{pd}}$  are the orbital temperature anomaly and precipitation ratio relative to the present day (not shown, see Banderas et al. (2017)), respectively, obtained from previous equilibrium simulations for the preindustrial and LGM climates performed with the CLIMBER-3 $\alpha$  model (Montoya and Levermann, 2008).  $\Delta \mathbf{T}_{\text{mil}}^{\text{atm}} = \mathbf{T}_{\text{is}}^{\text{atm}} - \mathbf{T}_{\text{st}}^{\text{atm}}$  and  $\delta \mathbf{P}_{\text{mil}} = \mathbf{P}_{\text{is}} / \mathbf{P}_{\text{st}}$  are the millennial temperature anomaly and precipitation ratio, respectively, for the interstadial relative to the stadial state (Section 2.3). **Rev. 1 SC 2: The key differences between these climate modes are that in the stadial, North Atlantic Deep Water (NADW) formation is relatively weak and takes place south of Iceland. Accordingly the sea-ice front in the North Atlantic reaches 40°N. In the interstadial state there is a northward shift and intensification of NADW formation. Northward oceanic heat transport increases, and the North Atlantic and surrounding areas warm relative to the stadial state, in particular the Nordic Seas. The simulated interstadial state is thus characterised by a more vigorous NADW formation and AMOC together with reduced sea ice in the Nordic Seas, and a temperature increase of up to 10 K in the North Atlantic relative to the stadial state, with a maximum anomaly in the Nordic Seas.** Note bold symbols indicate two-dimensional spatial fields. The stadial mode in our study is represented by a climate simulation of the LGM with CLIMBER-3 $\alpha$  (Montoya and Levermann, 2008). The interstadial mode is taken from a recent glacial transient simulation performed with the same model under glacial climatic conditions, but with intensified NADW formation (Banderas et al., 2015).  $\alpha^*$  and  $\beta^*$  are two indices that separately modulate the contribution of the orbital and millennial anomalies. Both

were built based on two recent complementary temperature reconstructions over Greenland, one from the NGRIP ice-core record for the LGP (Kindler et al., 2014), and the other one from several ice-core records for the Holocene (Vinther et al., 2009). Their combination (hereafter, the KV reconstruction) results in a continuous temperature reconstruction for Greenland for the past 120 ka (Banderas et al., 2017).  $\alpha^*$  is obtained after applying a low-pass frequency filter ( $f_c = 1/18 \text{ ka}^{-1}$ ) to the original KV reconstruction based on a spectral decomposition;  $\beta^*$  is obtained following a similar procedure but retaining the high frequency signal. Both indices are tuned in such a way that the resulting synthetic temperature time series at the NGRIP site exactly matches the KV reconstruction (this distinguishes  $\alpha^*$  and  $\beta^*$  from the raw  $\alpha$  and  $\beta$  indices previous to this tuning; Banderas et al. (2017)).

The net basal melting rate for floating parts  $B$  is assumed to follow a linear relation:

$$B = \kappa (T^{\text{ocn}} - T_f) \quad (3)$$

where  $T^{\text{ocn}}$  is the oceanic temperature close to the grounding line,  $T_f$  is the temperature at the ice base, assumed to be at the freezing point, and  $\kappa$  is the heat flux exchange coefficient between ocean water and ice at the ice-ocean interface. **Rev. 2 SC 15, 29 and 32** Several marine-shelf basal melting parameterizations can be found in the literature. The submarine melt rate is thought to be directly influenced by the oceanic temperature variations below the ice shelves. Accordingly, most basal melting parameterizations are built as a function of the difference between the oceanic temperature at the ice–ocean boundary layer and the temperature at the ice-shelf base, generally assumed to be at the freezing point. The dependence on this temperature difference can be linear (Beckmann and Goosse, 2003) or quadratic (Holland et al., 2008; Pollard and DeConto, 2012; DeConto and Pollard, 2016; Pattyn, 2017). The linear marine-shelf basal melting parameterization used in this study is the simplest case that allows testing of the ice-sheet sensitivity to past oceanic temperature changes. Nevertheless, it accounts separately for sub-ice-shelf areas near the grounding line and for purely floating ice (ice shelves). The basal melting rate for purely floating ice shelves ( $B_{\text{sh}}$ ) is given by the grounding-line basal melt  $B_{\text{gl}}$  scaled by a constant factor

$$B_{\text{sh}} = \gamma B_{\text{gl}}(t) \quad (4)$$

In this study,  $\gamma$  is set to 0.1. Thus, we consider that the submarine melting rate for ice shelves is 10 times lower than that close to the grounding zone, which is qualitatively in agreement with observations in some Greenland glaciers (Münchow et al., 2014; Rignot and Jacobs, 2002; Wilson et al., 2017). The melt rate in the open ocean, that is considered as being beyond the continental shelf break, is prescribed to a high value ( $20 \text{ m a}^{-1}$ ) to avoid unrealistic ice growth beyond 750 m of ocean depth, following Peyaud et al. (2007).

Following the approach described above,  $T^{\text{ocn}}(t)$  is assumed to be given by an expression analogous to Eq. 1. Thus Eq. 3 can be rewritten as:

$$B = B_0 + \kappa [(1 - \alpha^*(t)) \Delta T_{\text{orb}}^{\text{ocn}} + \beta^*(t) \Delta T_{\text{mil}}^{\text{ocn}}] \quad (5)$$

where  $B_0 = \kappa (T_0^{\text{ocn}} - T_f)$  represents the present-day oceanic basal melting rate.

**Rev. 2 GC4, SC2 and SC17:** Finally, millennial-scale sea-level variations are prescribed according to the reconstruction by Grant et al. (2012, Section 2.3). The specific details of the experimental setup used are described below.

### 2.3 Experimental setup

We herein investigate the response of the EIS to millennial-scale climate variability during MIS 3. The starting point of our experiments is a control-run ice-sheet simulation with constant boundary conditions for MIS 3 that provides a representative configuration of the EIS for that time period (Figure 1). To this end,  $\alpha^*$  was set to its value at 40 ka BP, that is,  $\alpha^* = \alpha_{40K}^* = -0.1$ , and  $\beta^* = 0$  to preclude millennial-scale variations. Note however these values are to a certain extent arbitrary; they are intended to provide a stable mean background state similar but not necessarily identical to background MIS 3 conditions. Thus:

$$T_{40K}^{\text{atm}} = T_0^{\text{atm}} + (1 - \alpha_{40K}^*) \Delta T_{\text{orb}}^{\text{atm}} \quad (6)$$

$$P_{40K} = P_0 [\alpha_{40K}^* + (1 - \alpha_{40K}^*) \delta P_{\text{orb}}] \quad (7)$$

$$10 \quad B_{40K} = B_0 + \kappa (1 - \alpha_{40K}^*) \Delta T_{\text{orb}}^{\text{ocn}} \quad (8)$$

Note that although Eq. 8 is formally correct and consistent with the scheme used, in contrast to the present-day SAT or precipitation the present-day rate of oceanic basal melting cannot be determined. Thus, in practice we replace this equation by directly tuning the value of  $B_{40K}$  to obtain a reasonable ice-sheet configuration at 40 ka BP given the atmospheric forcing fields expressed by equations 6-7. To this end, a constant basal melting rate of  $0.1 \text{ m a}^{-1}$  is assumed. **Rev. 1 SC 3: The ice sheet was forced with the resulting climatologies for 100 kyr previous to the starting of the perturbations described below. This allows the vertical temperature profile within the ice sheet to be equilibrated with the climate.** This procedure was found to facilitate the growth of European ice-sheets to an extent that satisfactorily agrees with previous reconstructions (Svendsen et al., 2004; Kleman et al., 2013).

Our forcing method allows to investigate the response of the EIS solely to millennial-scale climate variability at MIS 3 by keeping constant the orbital component of the forcing ( $\alpha^* = \alpha_{40K}^*$ ) and letting  $\beta^*$  vary throughout the LGP (eqs. 1, 2 and 5). In order to assess the relative roles of the atmosphere and the ocean, three independent experiments have been carried out. First, an atmospheric-only forced simulation (ATM) in which the time evolution of SAT and precipitation on millennial time scales is considered, while the oceanic forcing is kept constant to MIS 3 (i.e., 40 ka BP) background climatic conditions. Thus:

$$T^{\text{atm}}(t) = T_{40K}^{\text{atm}} + \beta^*(t) \Delta T_{\text{mil}}^{\text{atm}} \quad (9)$$

$$25 \quad P(t) = P_{40K} [(1 - \beta^*(t)) + \beta^*(t) \delta P_{\text{mil}}] \quad (10)$$

$$B(t) = B_{40K} \quad (11)$$

Second, an oceanic-only forced simulation OCN in which the atmospheric forcing is kept constant while the oceanic basal melting is allowed to vary at millennial timescales around its background MIS 3 value:

$$T^{\text{atm}}(t) = T_{40K}^{\text{atm}} \quad (12)$$

$$30 \quad P(t) = P_{40K} \quad (13)$$

$$B(t) = B_{40K} + \kappa \beta^*(t) \Delta T_{\text{mil}}^{\text{ocn}} \quad (14)$$

The magnitude and sign of oceanic temperature anomalies  $\Delta T^{\text{ocn}}$  depends on the depth at which  $T^{\text{ocn}}$  is considered. In our simulations, a large part of the NE sector of the EIS **Rev 1 GC4 and Rev 2 GC9**: is marine based with shallow bedrock depths between 500 m and less than 100 m in several locations further south. It is therefore unknown whether this marine ice sheet was more susceptible to changes in the surface or the subsurface of the ocean. To investigate the effect of this uncertainty, we decided to perform two different simulations considering different depths: one corresponding to the surface (OCNsrf) and the other one considering deeper (subsurface) oceanic waters by averaging temperatures within the range of 400-600 m depth (OCNsub). Therefore we hereafter distinguish between  $\Delta T_{\text{mil}}^{\text{ocn}}$  for surface or subsurface millennial-scale temperature anomalies, respectively (Figure 2). The realism and convenience of applying one or the other is addressed in section 5.

Finally, a simulation ALL combining both the atmospheric and the oceanic forcings:

$$10 \quad T^{\text{atm}}(t) = T_{40K}^{\text{atm}} + \beta^*(t) \Delta T_{\text{mil}}^{\text{atm}} \quad (15)$$

$$P(t) = P_{40K} [(1 - \beta^*(t)) + \beta^*(t) \delta P_{\text{mil}}] \quad (16)$$

$$B(t) = B_{40K} + \kappa \beta^*(t) \Delta T_{\text{mil}}^{\text{ocn}} \quad (17)$$

In all experiments  $\beta^*(t)$  dictates the millennial-scale variability of the forcings (Figure 3). Because our simulated stadial-to-interstadial transition results from an intensification of the AMOC, positive  $\beta^*$  values imply an increase in  $T^{\text{atm}}$  relative to its background MIS 3 value (e.g., Eq. 15 and Figures 2 and 3). As a consequence, the atmosphere warms at interstadials relative to stadial periods, as reflected by the  $\Delta T_{\text{mil}}^{\text{atm}}$  millennial-scale anomaly field (Figure 2). **Rev 2 GC1**: Note that for  $\kappa \beta^* \Delta T_{\text{mil}}^{\text{ocn}} < -B_{40K}$  refreezing is allowed ( $B(t) < 0$ ). Following Obase et al. (2017) in order to avoid unrealistic values of ice accretion under the ice shelves the sensitivity to the ocean is decreased by one order of magnitude when basal melting becomes negative, i.e., the refreezing rate is reduced to 10% of its estimated value following Eq. 5.:

$$20 \quad \kappa = \begin{cases} \kappa_0 & \text{if } B(t) > 0 \\ 0.1 \cdot \kappa_0 & \text{if } B(t) < 0 \end{cases} \quad (18)$$

where  $\kappa_0$  is the nominal value of the heat exchange coefficient. An ensemble of simulations for different values of  $\kappa_0$  have been considered to evaluate the sensitivity of the EIS to the forcing. **Rev. 2 GC4, SC2 and SC17**: Finally, varying sea-level forcing is considered (Figure 3b), both alone (SL run) and in combination with the previous forcings (ATM+OCN+SL).

### 3 Results

25 Substantial differences are found in the response of the EIS to the forcing scenarios. **Rev. 2 GC4, SC2 and SC17**: Under constant forcing, the CTRL run shows negligible millennial-scale sea-level equivalent (SLE) variations, although a lower frequency SLE fluctuation is found related to internal ice-sheet variability (Figure 3). **Rev. 1 SC17, Rev. 2 GC4**: When the model is forced only by changes in sea level (SL run), a slight response is observed on millennial-scales. These changes appear not be sufficient to cause a substantial migration of the grounding line, thus not affecting ice velocities. In ATM, the atmospheric forcing alone causes a sequence of enhanced ablation episodes resulting in modest ice volume variations (up to

1.5 m SLE) during the most prominent stadial-interstadial transitions. In contrast, **Rev. 1 GC4 and Rev 2 GC9:** the oceanic forcing in OCNsrf induces pronounced changes in the dynamics of the EIS on millennial time scales, with episodes of a large volume reduction occurring during interstadials. The combination of sea level, atmospheric and oceanic forcings (SL + ATM + OCNsrf run) results in a similar response of the EIS to that obtained in OCNsrf (Figure 3) as a consequence of the larger effect of the oceanic forcing in OCNsrf with respect to ATM. OCNsub shows an anti-phase relationship with respect to OCNsrf, with the largest reductions in ice volume occurring during prolonged stadial periods and regrowth phases happening during interstadials. This behavior can be explained by the fact that ocean waters at the subsurface warm (cool) during episodes of reduced (enhanced) convection at the Nordic Seas as a result of variations in the AMOC strength. Thus, the out-of-phase relationship found in the dynamic response of the EIS among these two oceanic experiments relates to the opposed sign of their spatial forcing patterns (Figure 2). When considering the forcing at the subsurface of the ocean together with the atmosphere (SL+ATM+OCNsub), slight reductions of the EIS volume (less than 1 m of s.l.e) during interstadials are superimposed onto the previous behavior (Figure 3).

**Rev2 GC1:** The magnitude of these changes for the MIS 3 period is illustrated in Figure 4. The simulation forced with the surface of the ocean (OCNsrf) and that including the rest of the forcings (OCNsrf + ATM + SL) show the largest amplitudes, with peaks of sea-level rise above  $4\text{ mm yr}^{-1}$  during DO-events and sustained contributions well above  $1\text{ mm yr}^{-1}$  during entire interstadial periods. In ATM, a decline of the EIS during stadial-to-interstadial transitions is still observed but presents a smaller amplitude of  $1\text{-}2\text{ mm yr}^{-1}$ . The simulations in which the ice sheet is forced with the subsurface of the ocean present a decline of their volume during stadial periods and regrowth during interstadials as a consequence of the inverted spatial pattern of temperature anomalies with respect to the surface. In the case of OCNsub the amplitude of these changes is smaller than in the OCNsrf case, on the order of  $0.5\text{-}1\text{ mm yr}^{-1}$ , and reaches more than  $1\text{ mm yr}^{-1}$  during pronounced stadials (as ca. at 44 ka BP). The OCNsub + ATM + SL simulation shows a slight volume loss during interstadials, as a consequence of the atmospheric forcing, that is superimposed onto the OCNsub behaviour.

**Rev 1 GC 5:** The response of the EIS has been analyzed in terms of its mass balance decomposition for the all-forcing runs (Figure 5). The surface ocean temperature varies in phase with the atmosphere. Thus, during stadial-to-interstadial transitions the high negative values of  $dV/dt$  can be explained by the conjunction of an initial sharp increase in ablation together with pronounced increases in basal melting and calving, which allow a large grounding line retreat in the Bjørnøyrenna basin (Figure 5 mid panel). The rate of ice loss by basal melting is similar to that resulting from the increase in ablation (as reflected in the surface mass balance) during the peak of a stadial-to-interstadial period. However, basal melting is much more efficient than surface mass balance in decreasing volume along the whole duration of an interstadial. This is due to the fact that ablation is restricted to the southern borders of the EIS. Thus, when the ice sheet has retreated to areas of no ablation, in spite of a slight further loss provided by the elevation feedback it rapidly equilibrates and a negative surface mass balance can not propagate further inland. In contrast, when enhanced basal melting from higher oceanic temperatures is applied, the associated retreat can propagate further inland occupying a large proportion of the Bjørnøyrenna basin and facilitating high rates of volume loss (although similar in amplitude with respect to SMB) during the whole interstadial period (see the animation in the Supplementary Information). **Rev. 2 SC 16:** During stadial periods, both enhanced positive mass balance and negative oceanic

anomalies (producing a slight refreezing) favor the regrowth of the EIS. Subsurface ocean temperatures evolve also in phase with the atmosphere in the SW part of the EIS but in anti-phase in its NE part. In other words, when forcing with the subsurface of the ocean, a slight warming (cooling) is observed around the Britain ice sheet while cooling (warming) of the Bjørnøyrenna basin is simulated during interstadial (stadial) periods (see Figure 2). Therefore, the OCNsub + ATM + SL simulation presents

5 volume declines during stadial-to-interstadial transitions due to an increase in ablation and basal melting in the SW part. **Rev. 2 SC 16:** Subsequently, reduced basal melting in the NE part of the EIS (allowing even a slight refreezing at its grounding line) favors regrowth of the Bjørnøyrenna basin during interstadial periods. Finally, shifting to pronounced stadial periods (as in ca. 44 ka BP) favors the penetration of warm subsurface waters that increase basal melting enough to produce an ice-sheet retreat in the NE part in spite of the enhanced positive surface mass balance. When considering the atmosphere and the subsurface ocean

10 forcing together, these competing processes translate into a smaller amplitude of millennial-scale EIS changes as compared to the case with surface ocean forcing. Furthermore, declines of the EIS can be observed both during the beginning of interstadial periods and during pronounced stadial periods in OCNsub + ATM + SL.

**Rev1 GC4 and Rev2 GC 9:** Focusing on the OCN and ATM simulations separately facilitates isolating the effects of the ocean on this complex pattern. To this end, the simulated ice-sheet distribution and velocities of OCNsrf, OCNsub and ATM

15 are shown in Figure 6 for the period around DO-event 12, at ca. 47 ka BP. As expected, OCNsrf shows a widespread retreat both in the NE and the SW of the EIS from the stadial to the interstadial period. This is accompanied by an acceleration of the Bjørnøyrenna basin due to its grounding line thinning and retreat (Figure 6, left panels). OCNsub presents a collapsed Bjørnøyrenna basin during the stadial period previous to DO-event 12 due to enhanced basal melting from warmer subsurface waters. The transition to the interstadial period favors the regrowth of this NE part of the EIS due to decreased basal melting,

20 while its SW section slightly retreats (Figure 6 mid panels). Concerning ATM, only in the southwestern (SW) part of the EIS is the atmospheric forcing capable of generating an important reduction in the EIS volume in response to the stadial-interstadial transition (Figure 6 right panels). This is a result of the spatial pattern of the forcing, with the largest SAT anomalies located around the Nordic seas (Figure 2). Therefore, the ice volume reduction of the EIS in ATM is due to the positive SAT anomaly, which leads to enhanced ablation in the SW part of the EIS. In turn, reduced SATs during stadials allow the regrowth of the ice

25 sheet up to the continental margin of the Nordic seas. The more active dynamic response of the EIS in OCN simulations can be attributed to the increase in oceanic temperatures by 2-4°C (Figure 2) within the margins of the ice-sheet during interstadial (in the case of OCNsrf) and stadial (OCNsub case) periods, which translates into enhanced basal melting at the margins of the EIS. The SW sector of the EIS also responds to the warmer SSTs, actually with a larger reduction of ice volume than in ATM (Figure 6).

30 The spatial patterns shown in Figure 6 are representative of the stadial-to-interstadial transitions. **Rev1 GC4 and Rev1 SC9:** In OCNsrf, the EIS reacts to every abrupt surface warming with a substantial ice-flow acceleration, especially in the Bjørnøyrenna basin (Figure 7). Ice shelves that are present during stadial periods suddenly retreat during DO-events and together with enhanced basal melting favor thinning and retreat of the grounding line that translate in large iceberg discharges up to ca. 0.06 Sv. In the OCNsub case, ice velocities in the Bjørnøyrenna basin increase during stadials, when enhanced basal melting erodes the grounding line and favors its retreat. Peaks in calving are recorded accordingly during pronounced stadial

35

periods. These peaks are however of less amplitude than in the OCNsrf case. This can be explained by the fact that transitions to stadials are usually more gradual than transitions to interstadials, thus the incursion of warmer waters happens in this case in a smoother manner. High velocities reach their maxima at the end of the stadial and beginning of the interstadials. The latter are however not accompanied by an increase in calving due to the fact that ice shelves are expanding and thickening during this period thanks to reduced basal melting (Figure 8). In general, the extension of ice shelves is greatly reduced during periods of enhanced basal melting (Figures 7, 8), with no large unconfined ice shelves surviving during these episodes (see the Supplementary Information). Some thinner ice shelves remain, in spite of the enhanced basal melting, thanks to an increase in advection from the Bjørnøyrenna ice stream triggered by a grounding line retreat (Figure 6).

**Rev. 1 SC 11:** Note that changes in the position of the calving front are usually accompanied by a grounding line displacement. For some minor ice-shelf breakups this close relationship can be broken, but with almost no effects upstream inland. Thus we consider that the grounding line position is the best indicator for characterizing the dynamic behavior of the marine part of the EIS.

Inspection of the temporal evolution of the grounding line position in OCN simulations confirms that ice dynamics control the majority of ice-volume variations in the EIS as opposed to the SMB processes involved in ATM. The migration of the grounding line through time has been characterized by means of an index ( $\mu$ ) that weighs the proportion of non-grounded points in the region of the Bjørnøyrenna basin:

$$\mu(t) = \left(1 - \frac{N_g(t)}{N}\right) \cdot 100 \quad (19)$$

where  $N_g(t)$  represents the evolution of the number of points of grounded ice within a fixed area of  $N$  points in the Barents Sea region. While in ATM  $\mu$  barely changes (Figure 9), OCN runs show a large dynamic behavior of the basin. **Rev1 GC4 and Rev1 SC9:** In OCNsrf,  $\mu$  reflects a synchronous evolution of the grounding line position and the oceanic forcing, with major retreats coinciding with interstadial states (Figure 9). Conversely, the Bjørnøyrenna basin is generally much closer to a full retreat in OCNsub due to a larger penetration of warm subsurface waters (Figure 2, right compared to 2, middle) during stadials. However, the grounding line is able to advance and reach Svalbard during episodes of reduced basal melting at the interstadials (Figure 9).

The direct coupling between the oceanic forcing and the response of the Bjørnøyrenna ice stream is also evident from the relatively high negative correlation ( $r \simeq -0.70$ ) found between  $\mu$  and ice thickness (Figure 9). In essence, in response to the grounding-line retreat (advance), acceleration (deceleration) of the flow takes place upstream in the Bjørnøyrenna ice stream, as reflected by the nearly linear positive correlation ( $r \simeq 0.93$ ) found between  $\mu$  and velocities in the channel (Figure 9). (Figure 7).

**The only thing left: ADD OCNsub in figure 9, and describe it.**

**Rev1 GC1 and Rev2 SC1:** As a consequence of the destabilization of the ice sheet, important ice-volume variations are observed in the NE part of the EIS during millennial-scale climatic transitions, which added to the minor contribution of the SW retreat, result in fluctuations of more than 4 m SLE in OCNsrf, up to 2.5 m in OCNsub and ca. 1 m in ATM (Figure 3).

In order to investigate the sensitivity of the results to the model parameters, eight additional OCN simulations, both for the surface and the subsurface, have been carried out with different  $\kappa_0$  parameters between  $1-9 \text{ m a}^{-1} \text{ K}^{-1}$ , i.e., bracketing our standard case of  $\kappa_0 = 5 \text{ m a}^{-1} \text{ K}^{-1}$ . This choice reflects the inferences based on measurements made on Antarctic ice shelves that a variation of 1 K in the effective oceanic temperature changes the melt rate by ca.  $10 \text{ m a}^{-1}$  (Rignot and Jacobs, 2002; Shepherd et al., 2004). A robust response of the EIS is found, with a more reactive EIS response for increasing  $\kappa$  values (see Supplementary Information). The sensitivity of our results to the values of the atmospheric mass balance model has also been explored. In spite of largely exploring the values of the parameters that determine the sensitivity to surface mass balance, the EIS variability induced by the ocean is always found to be of greater amplitude than the one induced by the atmosphere provided that  $\kappa_0 > 3 \text{ m a}^{-1} \text{ K}^{-1}$  (see Supplementary Information).

## 10 4 Discussion

Our results suggest a highly dynamic Eurasian ice sheet at millennial time-scales largely responding to changes in the ocean temperatures. **Rev. 2 GC 4:** Some authors present the marine based Kara-Barents complex as an analogue for present-day West Antarctic ice sheet for which bedrock topography is a major control for stability. Marine ice sheet instability is generally triggered by a sub-shelf basal melt perturbation but is largely amplified by the local bedrock depth. We have shown, in this sense, that the Bjørnøyrenna basin is highly susceptible to changes in the oceanic temperatures. The timing of this response with respect to changes registered in Greenland depends, however, on whether the surface or the subsurface of the ocean is considered as the relevant forcing of the ice sheet.

Recently, IRD peaks of Fennoscandian origin reported from a high-resolution marine sediment core from the Norwegian Sea indicate the presence of more frequent IRD deposition and thus calving during interstadials than during stadials (Dokken et al., 2013). This result has been corroborated in a compilation of new and previously published data (Becker et al., 2017) clearly showing that within MIS 3, the IRD deposition increases within interstadials. The coeval deposition of carbonate-rich, sorted fine sands and near-surface warming suggests the presence of Atlantic water along the margin, and is interpreted by the authors as the effects of winnowing due to an intensified AMOC during interstadials. This interpretation results in concordance with our results when considering the surface waters as the oceanic forcing. Thus, this agreement would play in favor of considering that the EIS was primarily responding to changes in the surface of the ocean.

Our results also provide a mechanism to explain the pervasive presence of IRD in the North Atlantic during MIS 3, both during stadials and interstadials, and originating both in the LIS and the EIS. During stadials, the simultaneous appearance of IRD across the wider North Atlantic Ocean can be explained through the build-up of subsurface heat in the high-latitude North Atlantic leading to increased iceberg calving in the presence of large, thick ice shelves, together with lower surface temperatures allowing for wider dispersal of icebergs (Barker et al., 2015). According to our results interstadials could lead to enhanced calving of the EIS through oceanic surface subglacial melting as a result of the warmer surface conditions and relatively shallow grounding line of this ice sheet.

The identification of IRD layers with increased calving through ice-sheet instabilities must be taken with caution, since it is based on several untested assumptions (Clark and Pisias, 2000): (i) delivery of IRD to a specific site is caused solely by iceberg calving, versus transport by sea-ice; (ii) an increase in IRD represents an increase in the iceberg flux, versus a greater amount of debris incorporated at the base of the ice sheet that delivers the icebergs, or a greater distance of iceberg transport; (iii) the amount of IRD carried by all the icebergs is similar, assuming therefore a direct relationship between IRD concentration and iceberg flux. However, the former assumptions have not been confirmed and, thus, the calving-IRD relationship might not be so direct. In addition, ocean temperatures affect melting of icebergs and thus their release of IRD. Variations in ocean temperatures can alter the IRD released by an iceberg at a certain site, causing variations in IRD deposition even for a constant amount of icebergs produced at the source.

Our experimental setup is not intended to match the paleorecord, but to provide insight into the response of the EIS to millennial-scale variability. The EIS variations simulated here represent the upper-end amplitude of potential responses during the whole glacial cycle, due to its large size. Extending the study to cover the whole LGP would require the consideration of orbital variability as part of the forcing. In this case, the EIS would likely be smaller during the mildest phase of MIS 3, thus limiting its contact with the ocean and the production of iceberg discharges.

Also, our results depend somewhat on the particular SAT and **Rev 1 GC 4: oceanic temperature** anomaly patterns simulated by our climate model, the magnitudes of the resulting forcing, and the initial size of the simulated EIS. **Rev 1 GC 1: The use of different atmospheric realisations is subject to the availability of climate simulations with different models for the three climate states needed: glacial (stadial), present, and interstadial. The latter is only available for a reduced number of models. This makes the assessment of this issue difficult in the present study.** Assessing the sensitivity to these features should be in the scope of future work, and illustrates the need for carrying out new simulations of both the interstadial and the stadial states with more sophisticated climate models. **Rev. 2 SC1: Nonetheless, our results indicate that the ocean is the major driver of the EIS ice-volume changes during MIS-3. Note the temporal index used is the same for the atmosphere and the ocean and the amplitude is given by an OGCM simulation of two different oceanic states mimicking stadial and interstadial periods. We then translate those fields into ablation (through PDD, whose uncertainty has been extensively explored) and into basal melting (through a linear equation). The values of the oceanic sensitivity parameter ( $\kappa$ ) we used here are in the range (or even below in most cases) of those suggested by data in Antarctica (Rignot et al. 2002). Note, in particular, that even for low-mid values of  $\kappa$  of 3 meter/year/Kelvin the response to the ocean appears to be of greater amplitude than that to the atmosphere, making our main conclusions robust** Finally, our study lacks bi-directional coupling between the ice sheet, the atmosphere and the ocean. Eventually the goal is to investigate this matter with fully coupled climate-ice sheet models.

Meltwater discharge from the EIS and other ice sheets surrounding the Nordic Seas is often implied as a cause of ocean instabilities. The same would be the case for iceberg discharges. This issue is beyond the scope of this study; its assessment would require investigating the impact of these freshwater perturbations in deep water formation and the AMOC. Again, proper assessment requires the use of a coupled climate-ice sheet model.

## 5 Conclusions

We have investigated the response of the EIS to millennial-scale climate variability associated with DO-events through a series of simulations with a three-dimensional, hybrid ice-sheet model that represents inland ice flow under the SIA and floating ice shelves and ice streams through the SSA. The model makes use of an offline forcing method that separately accounts for orbital and millennial-scale climate variability during the LGP, improving the representation of the latter (Banderas et al., 2017). Atmospheric and ocean forcings associated with millennial-scale variability were considered both separately and together.

Separating the effects of atmospheric and oceanic forcing during the glacial period has allowed us to quantify the contribution of each to EIS variability. Atmospheric forcing during stadial-interstadial transitions has a **Rev2 SC1:very** modest effect on the ice sheet, which is a consequence of the largest SMB changes being confined to SW sector of the EIS, where the forcing is strongest. In contrast, the oceanic forcing has a **Rev2 SC1: much** larger effect, through changes in the ice dynamics in the **Bjørnøyrenna basin** of the EIS. Ocean warming is able to induce a retreat of grounded ice in this part of the EIS through dynamic processes. As a consequence, significant ice-volume variations result during millennial-scale climatic transitions. Added to the **Rev2 SC 18: smaller** contribution of the SW retreat, this results in sea-level changes on the order of several meters. Sensitivity experiments for different values of the oceanic heat coefficient parameter show that this is a robust response of the model.

Our results thus support the existence of a highly dynamic EIS during the LGP. They suggest an important role of oceanic melt forcing through changes in the ocean circulation in controlling the ice-stream activity. Together with previous work (Alvarez-Solas et al., 2013), they imply that oceanic circulation changes and the associated ocean-ice sheet interactions are able to explain virtually all ice rafting events in the North Atlantic within MIS 3, from the H-events of the LIS during stadials to those of the EIS during interstadials. **Additionally, our results highlight the need for stronger constraints on the local North Atlantic behavior in order to shed light on the ice sheet's glacial dynamics.**

*Competing interests.* The authors declare no competing interests

*Acknowledgements.* This work was funded by the Spanish Ministerio de Economía y Competitividad (MINECO) through project MOCCA (Modelling Abrupt Climate Change, Grant CGL2014-59384-R). R. Banderas was funded by a PhD Thesis grant of the Universidad Complutense de Madrid. A. Robinson is funded by the Marie Curie Horizon2020 project CONCLIMA (Grant 703251). Part of the computations of this work were performed in EOLO, the HPC of Climate Change of the International Campus of Excellence of Moncloa, funded by MECD and MICINN. This is a contribution to CEI Moncloa.

## References

- Alley, R. B., Clark, P. U., Huybrechts, P., and Joughin, I.: The deglaciation of the Northern Hemisphere: a global perspective, *Ann. Rev. Earth and Plan. Sci.*, 27, 149–182, doi: 10.1146/annurev.earth.27.1.149, 1999.
- Alvarez-Solas, J., Montoya, M., Ritz, C., Ramstein, G., Charbit, S., Dumas, C., Nisancioglu, K., Dokken, T., and Ganopolski, A.: Heinrich event 1: an example of dynamical ice-sheet reaction to oceanic changes, *Clim. Past*, 7, 1297–1306, <https://doi.org/10.5194/cp-7-1297-2011>, 2011.
- Alvarez-Solas, J., Robinson, A., Montoya, M., and Ritz, C.: Iceberg discharges of the last glacial period driven by oceanic circulation changes, *Proceedings of the National Academy of Sciences*, 110, 16350–16354, 2013.
- Amante, C. and Eakins, B. W.: ETOPO1 1 Arc-minute Global Relief Model: Procedures, Data Sources and Analysis, <https://doi.org/10.7289/V5C8276M>, 2009.
- Andreassen, K. and Winsborrow, M.: Signature of ice streaming in Bjørnøyrenna, Polar North Atlantic, through the Pleistocene and implications for ice-stream dynamics, *Annals of Glaciology*, 50, 17–26, <https://doi.org/10.3189/172756409789624238>, 2009.
- Bamber, J. L., Layberry, R. L., and Gogineni, S.: A new ice thickness and bed data set for the Greenland ice sheet: 1. Measurement, data reduction, and errors, *Journal of Geophysical Research: Atmospheres*, 106, 33 773–33 780, 2001.
- Banderas, R., Alvarez-Solas, J., Robinson, A., and Montoya, M.: An interhemispheric mechanism for glacial abrupt climate change, *Clim. Dyn.*, 44, 2897–2908, <https://doi.org/10.1007/s00382-014-2211-8>, 2015.
- Banderas, R., Alvarez-Solas, J., Robinson, A., and Montoya, M.: A new approach for simulating the paleo evolution of the Northern Hemisphere ice sheets, *Geoscientific Model Development Discussions*, 2017, 1–24, <https://doi.org/10.5194/gmd-2017-158>, <https://www.geosci-model-dev-discuss.net/gmd-2017-158/>, 2017.
- Barker, S., Chen, J., Gong, X., Jonkers, L., Knorr, G., and Thornalley, D.: Icebergs not the trigger for North Atlantic cold events, *Nature*, 520, 333, 2015.
- Becker, L. W., Sejrup, H. P., Hjelstuen, B. O., Hafliðason, H., and Dokken, T. M.: Ocean-ice sheet interaction along the SE Nordic Seas margin from 35 to 15ka BP, *Marine Geology*, 2017.
- Beckmann, A. and Goosse, H.: A parameterization of ice shelf-ocean interaction for climate models, *Ocean Modelling*, 5, 157–170, 2003.
- Bond, G., Broecker, W., Johnsen, S., McManus, J., Labeyrie, L., Jouzel, J., Bonani, G., et al.: Correlations between climate records from North Atlantic sediments and Greenland ice, *Nature*, 365, 143–147, <https://doi.org/10.1038/365143a0>, 1993.
- Bueler, E. and Brown, J.: Shallow shelf approximation as a “sliding law” in a thermomechanically coupled ice sheet model, *Journal of Geophysical Research: Earth Surface*, 114, 2009.
- Clark, P. U. and Pisias, N. G.: Interpreting iceberg deposits in the deep sea, *Science*, 290, 51–52, 2000.
- Clason, C. C., Applegate, P., and Holmlund, P.: Modelling Late Weichselian evolution of the Eurasian ice sheets forced by surface meltwater-enhanced basal sliding, *Journal of Glaciology*, 60, 29–40, 2014.
- Dansgaard, W., Johnsen, S., Clausen, H., Dahl-Jensen, D., Gundestrup, N., Hammer, C., Hvidberg, C., Steffensen, J., Sveinbjörnsdóttir, A., Jouzel, J., et al.: Evidence for general instability of past climate from a 250-kyr ice-core record, *Nature*, 364, 218–220, <https://doi.org/10.1038/364218a0>, 1993.
- DeConto, R. M. and Pollard, D.: Contribution of Antarctica to past and future sea-level rise, *Nature*, 531, 591, 2016.

- Dee, D., Uppala, S., Simmons, A., Berrisford, P., Poli, P., Kobayashi, S., Andrae, U., Balmaseda, M., Balsamo, G., Bauer, P., et al.: The ERA-Interim reanalysis: Configuration and performance of the data assimilation system, *Quarterly Journal of the Royal Meteorological Society*, 137, 553–597, 2011.
- Dokken, T. M., Nisancioglu, K. H., Li, C., Battisti, D. S., and Kissel, C.: Dansgaard-Oeschger cycles: Interactions between ocean and sea ice intrinsic to the Nordic seas, *Paleoceanography*, 28, 491–502, <https://doi.org/10.1002/palo.20042>, 2013.
- 5 Forsström, P.-L. and Greve, R.: Simulation of the Eurasian ice sheet dynamics during the last glaciation, *Global and Planetary Change*, 42, 59–81, 2004.
- Grant, K., Rohling, E., Bar-Matthews, M., Ayalon, A., Medina-Elizalde, M., Ramsey, C. B., Satow, C., and Roberts, A.: Rapid coupling between ice volume and polar temperature over the past 150,000 [thinsp] years, *Nature*, 491, 744–747, 2012.
- 10 Grousset, F. E., Pujol, C., Labeyrie, L., Auffret, G., and Boelaert, A.: Were the North Atlantic Heinrich events triggered by the behavior of the European ice sheets?, *Geology*, 28, 123–126, 2000.
- Gudlaugsson, E., Humbert, A., Winsborrow, M., and Andreassen, K.: Subglacial roughness of the former Barents Sea ice sheet, *Journal of Geophysical Research: Earth Surface*, 118, 2546–2556, 2013.
- Gudlaugsson, E., Humbert, A., Andreassen, K., Clason, C. C., Kleiner, T., and Beyer, S.: Eurasian ice-sheet dynamics and sensitivity to subglacial hydrology, *Journal of Glaciology*, 63, 556–564, 2017.
- 15 Hall, I. R., Colmenero-Hidalgo, E., Zahn, R., Peck, V. L., and Hemming, S.: Centennial-to millennial-scale ice-ocean interactions in the subpolar northeast Atlantic 18–41 kyr ago, *Paleoceanography*, 26, 2011.
- Heinrich, H.: Origin and consequences of cyclic ice rafting in the northeast Atlantic Ocean during the past 130,000 years, *Quaternary Research*, 29, 142–152, [https://doi.org/10.1016/0033-5894\(88\)90057-9](https://doi.org/10.1016/0033-5894(88)90057-9), 1988.
- 20 Helmens, K. F. and Engels, S.: Ice-free conditions in eastern Fennoscandia during early Marine Isotope Stage 3: lacustrine records, *Boreas*, 39, 399–409, 2010.
- Hemming, S. R.: Heinrich events: Massive late Pleistocene detritus layers of the North Atlantic and their global climate imprint, *Rev. Geophys.*, 42, RG1005, <https://doi.org/10.1029/2003RG000128>, 2004.
- Holland, P. R., Jenkins, A., and Holland, D. M.: The response of ice shelf basal melting to variations in ocean temperature, *Journal of Climate*, 21, 2558–2572, 2008.
- 25 Huber, C., Leuenberger, M., Spahni, R., Flückiger, J., Schwander, J., Stocker, T., Johnsen, S., Landais, A., and Jouzel, J.: Isotope calibrated Greenland temperature record over Marine Isotope Stage 3 and its relation to CH<sub>4</sub>, *Earth and Planetary Science Letters*, 243, 504–519, <https://doi.org/10.1016/j.epsl.2006.01.002>, 2006.
- Hughes, A. L., Gyllencreutz, R., Lohne, Ø. S., Mangerud, J., and Svendsen, J. I.: The last Eurasian ice sheets—a chronological database and time-slice reconstruction, DATED-1, *Boreas*, 45, 1–45, 2016.
- 30 Hutter, K.: *Theoretical glaciology: material science of ice and the mechanics of glaciers and ice sheets*, vol. 1, Springer, 1983.
- Kindler, P., Guillevic, M., Baumgartner, M., Schwander, J., Landais, A., and Leuenberger, M.: Temperature reconstruction from 10 to 120 kyr b2k from the NGRIP ice core, *Climate of the Past*, 10, 887–902, <https://doi.org/10.5194/cp-10-887-2014>, <http://www.clim-past.net/10/887/2014/>, 2014.
- 35 Kleman, J., Fastook, J., Ebert, K., Nilsson, J., and Caballero, R.: Pre-LGM Northern Hemisphere ice sheet topography, *Climate of the Past*, 9, 2365, 2013.
- Laske, G.: A global digital map of sediment thickness, *Eos Trans. AGU*, 78, F483, 1997.

- Lekens, W., Sejrup, H., Hafliðason, H., Knies, J., and Richter, T.: Meltwater and ice rafting in the southern Norwegian Sea between 20 and 40 calendar kyr BP: Implications for Fennoscandian Heinrich events, *Paleoceanography*, 21, 2006.
- MacAyeal, D. R.: Large-scale ice flow over a viscous basal sediment: Theory and application to ice stream B, Antarctica, *Journal of Geophysical Research: Solid Earth*, 94, 4071–4087, 1989.
- 5 Mangerud, J., Løvlie, R., Gulliksen, S., Hufthammer, A.-K., Larsen, E., and Valen, V.: Paleomagnetic correlations between scandinavian ice-sheet fluctuations and greenland dansgaard–oeschger events, 45,000–25,000 yr BP, *Quaternary Research*, 59, 213–222, 2003.
- Mangerud, J., Gulliksen, S., and Larsen, E.: 14C-dated fluctuations of the western flank of the Scandinavian Ice Sheet 45–25 kyr BP compared with Bølling–Younger Dryas fluctuations and Dansgaard–Oeschger events in Greenland, *Boreas*, 39, 328–342, 2010.
- Marshall, S. J. and Koutnik, M. R.: Ice sheet action versus reaction: Distinguishing between Heinrich events and Dansgaard-Oeschger cycles  
10 in the North Atlantic, *Paleoceanography*, 21, 2006.
- Montoya, M. and Levermann, A.: Surface wind-stress threshold for glacial Atlantic overturning, *Geophys. Res. Lett.*, 35, L03 608, <https://doi.org/10.1029/2007GL032560>, 2008.
- Münchow, A., Padman, L., and Fricker, H. A.: Interannual changes of the floating ice shelf of Petermann Gletscher, North Greenland, from 2000 to 2012, *Journal of Glaciology*, 60, 489–499, 2014.
- 15 Obase, T., Abe-Ouchi, A., Kusahara, K., Hasumi, H., and Ohgaito, R.: Responses of Basal Melting of Antarctic Ice Shelves to the Climatic Forcing of the Last Glacial Maximum and CO<sub>2</sub> Doubling, *Journal of Climate*, 30, 3473–3497, 2017.
- Olsen, L., Sveian, H., Borg, K., Bergstram, B., and Broekmans, M.: Rapid and rhythmic ice sheet fluctuations in western Scandinavia 15-40 Kya—a review, *Polar Research*, 21, 235–242, 2002.
- Patton, H., Hubbard, A., Andreassen, K., Winsborrow, M., and Stroeven, A. P.: The build-up, configuration, and dynamical sensitivity of the  
20 Eurasian ice-sheet complex to Late Weichselian climatic and oceanic forcing, *Quaternary Science Reviews*, 153, 97–121, 2016.
- Pattyn, F.: Sea-level response to melting of Antarctic ice shelves on multi-centennial timescales with the fast Elementary Thermomechanical Ice Sheet model (f. ETISH v1. 0), *The Cryosphere*, 11, 1851, 2017.
- Peck, V., Hall, I., Zahn, R., Grousset, F., Hemming, S., and Scourse, J.: The relationship of Heinrich events and their European precursors over the past 60ka BP: a multi-proxy ice-rafted debris provenance study in the North East Atlantic, *Quaternary Science Reviews*, 26,  
25 862–875, 2007.
- Peyaud, V., Ritz, C., and Krinner, G.: Modelling the Early Weichselian Eurasian Ice Sheets: role of ice shelves and influence of ice-dammed lakes, *Climate of the Past Discussions*, 3, 221–247, 2007.
- Pollard, D. and DeConto, R.: Description of a hybrid ice sheet-shelf model, and application to Antarctica, *Geoscientific Model Development*, 5, 1273, 2012.
- 30 Rasmussen, T. L. and Thomsen, E.: Pink marine sediments reveal rapid ice melt and Arctic meltwater discharge during Dansgaard-Oeschger warmings, *Nature communications*, 4, 2849, 2013.
- Reeh, N.: Parameterization of melt rate and surface temperature on the Greenland ice sheet, *Polarforschung*, 59, 113–128, 1989.
- Rignot, E. and Jacobs, S. S.: Rapid bottom melting widespread near Antarctic ice sheet grounding lines, *Science*, 296, 2020–2023, 2002.
- Ritz, C., Rommelaere, V., and Dumas, C.: Modeling the evolution of Antarctic ice sheet over the last 420,000 years: Implications for altitude  
35 changes in the Vostok region, *Journal of Geophysical Research: Atmospheres* (1984–2012), 106, 31 943–31 964, 2001.
- Scourse, J. D., Hall, I. R., McCave, I. N., Young, J. R., and Sugdon, C.: The origin of Heinrich layers: evidence from H<sub>2</sub> for European precursor events, *Earth and Planetary Science Letters*, 182, 187–195, 2000.

- Scourse, J. D., Haapaniemi, A. I., Colmenero-Hidalgo, E., Peck, V. L., Hall, I. R., Austin, W. E., Knutz, P. C., and Zahn, R.: Growth, dynamics and deglaciation of the last British–Irish ice sheet: the deep-sea ice-rafted detritus record, *Quaternary Science Reviews*, 28, 3066–3084, 2009.
- Shapiro, N. M. and Ritzwoller, M. H.: Inferring surface heat flux distributions guided by a global seismic model: particular application to Antarctica, *Earth and Planetary Science Letters*, 223, 213–224, 2004.
- Shepherd, A., Wingham, D., and Rignot, E.: Warm ocean is eroding West Antarctic ice sheet, *Geophysical Research Letters*, 31, 2004.
- Siegert, M. J. and Dowdeswell, J. A.: Numerical reconstructions of the Eurasian Ice Sheet and climate during the Late Weichselian, *Quaternary Science Reviews*, 23, 1273–1283, 2004.
- Steffensen, J., Andersen, K., Bigler, M., Clausen, H., Dahl-Jensen, D., Fischer, H., Goto-Azuma, K., Hansson, M., Johnsen, S., Jouzel, J., Masson-Delmotte, V., Popp, T., Rasmussen, S., Röthlisberger, R., Ruth, U., Stauffer, B., Siggaard-Andersen, M., Sveinbjörnsdóttir, A., Svensson, A., and White, J.: High-Resolution Greenland Ice Core Data Show Abrupt Climate Change Happens in Few Years, *Science*, 321, 680–684, doi: 10.1126/science.1157707, 2008.
- Svendsen, J. I., Alexanderson, H., Astakhov, V. I., Demidov, I., Dowdeswell, J. A., Funder, S., Gataullin, V., Henriksen, M., Hjort, C., Houmark-Nielsen, M., et al.: Late Quaternary ice sheet history of northern Eurasia, *Quaternary Science Reviews*, 23, 1229–1271, 2004.
- Vinther, B. M., Buchardt, S. L., Clausen, H. B., Dahl-Jensen, D., Johnsen, S. J., Fisher, D., Koerner, R., Raynaud, D., Lipenkov, V., Andersen, K., et al.: Holocene thinning of the Greenland ice sheet, *Nature*, 461, 385–388, 2009.
- von Kreveld, S. v., Sarnthein, M., Erlenkeuser, H., Grootes, P., Jung, S., Nadeau, M., Pflaumann, U., and Voelker, A.: Potential links between surging ice sheets, circulation changes, and the Dansgaard-Oeschger cycles in the Irminger Sea, 60–18 kyr, *Paleoceanography*, 15, 425–442, 2000.
- Wilson, N., Straneo, F., and Heimbach, P.: Satellite-derived submarine melt rates and mass balance (2011–2015) for Greenland’s largest remaining ice tongues, *The Cryosphere*, 11, 2773, 2017.
- Wohlfarth, B.: Ice-free conditions in Sweden during Marine Oxygen Isotope Stage 3?, *Boreas*, 39, 377–398, 2010.

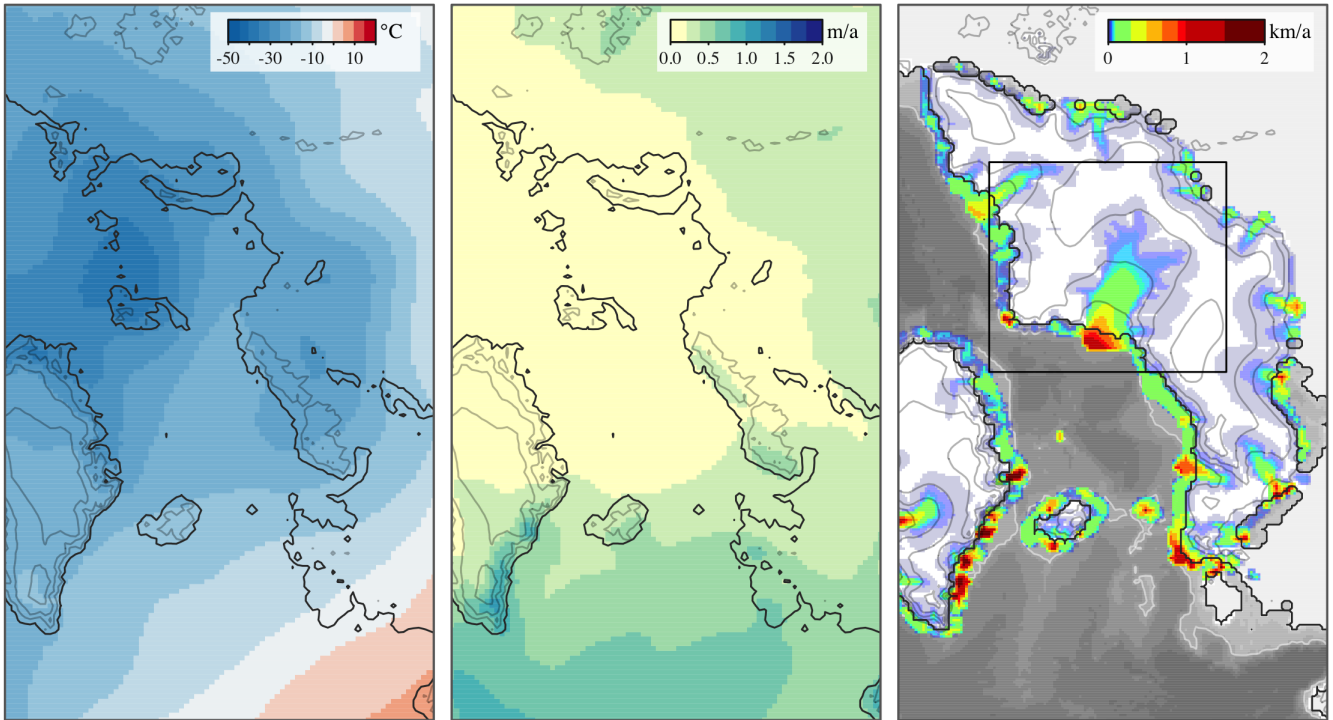


**Figure 1.** Background climatic forcing and resulting ice sheet for the control run CTRL. MIS 3 (~40 ka BP) reference annual mean SAT in  $^{\circ}\text{C}$  (left) and annual mean precipitation in  $\text{m a}^{-1}$  (middle). Present-day contour lines with the land boundary delineated at a depth of -80 m are added for reference. Simulated MIS 3 ice sheet distribution and velocities after the spinup was completed (right). This ice-sheet represents the initial state previous to the applied perturbations. Bjørnøyrenna basin, as referenced in the text, is shown by the black rectangle.

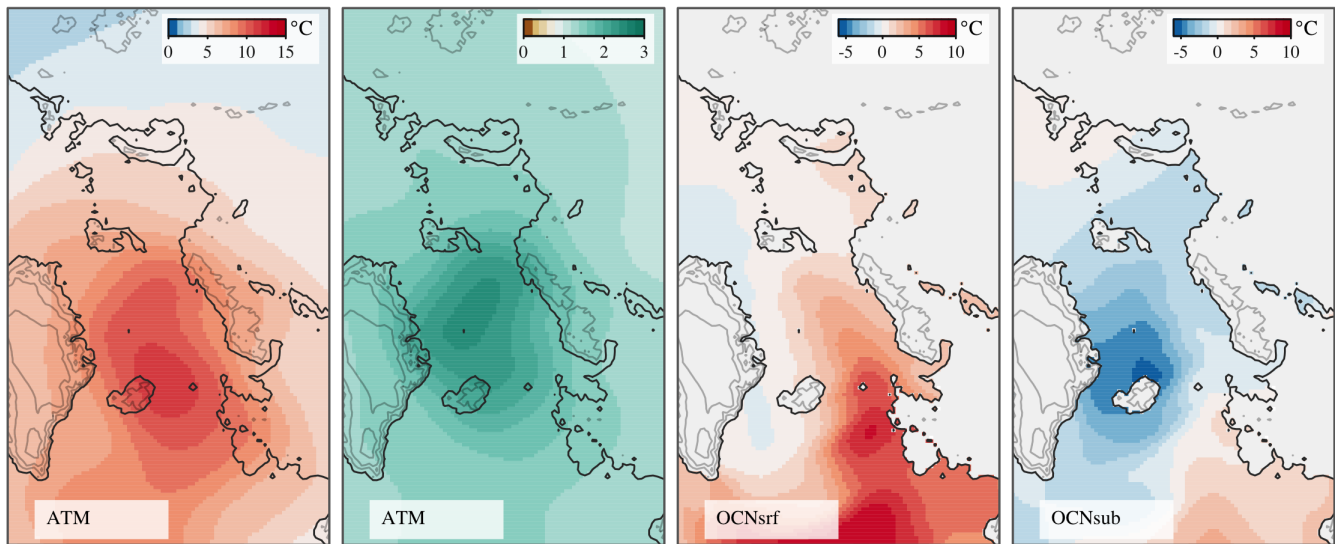


**Figure 2.** Millennial-scale components of the boundary forcing. **a)** SAT anomalies (interstadial minus stadial) in °C. **b)** precipitation ratio (interstadial to stadial). **c)** Anomalies of SST and **d)** subsurface ocean temperature (at 500 m depth) in °C corresponding to the millennial-scale oceanic component of the forcing. Present-day contour lines with the land boundary delineated at a depth of -80 m are added for reference.

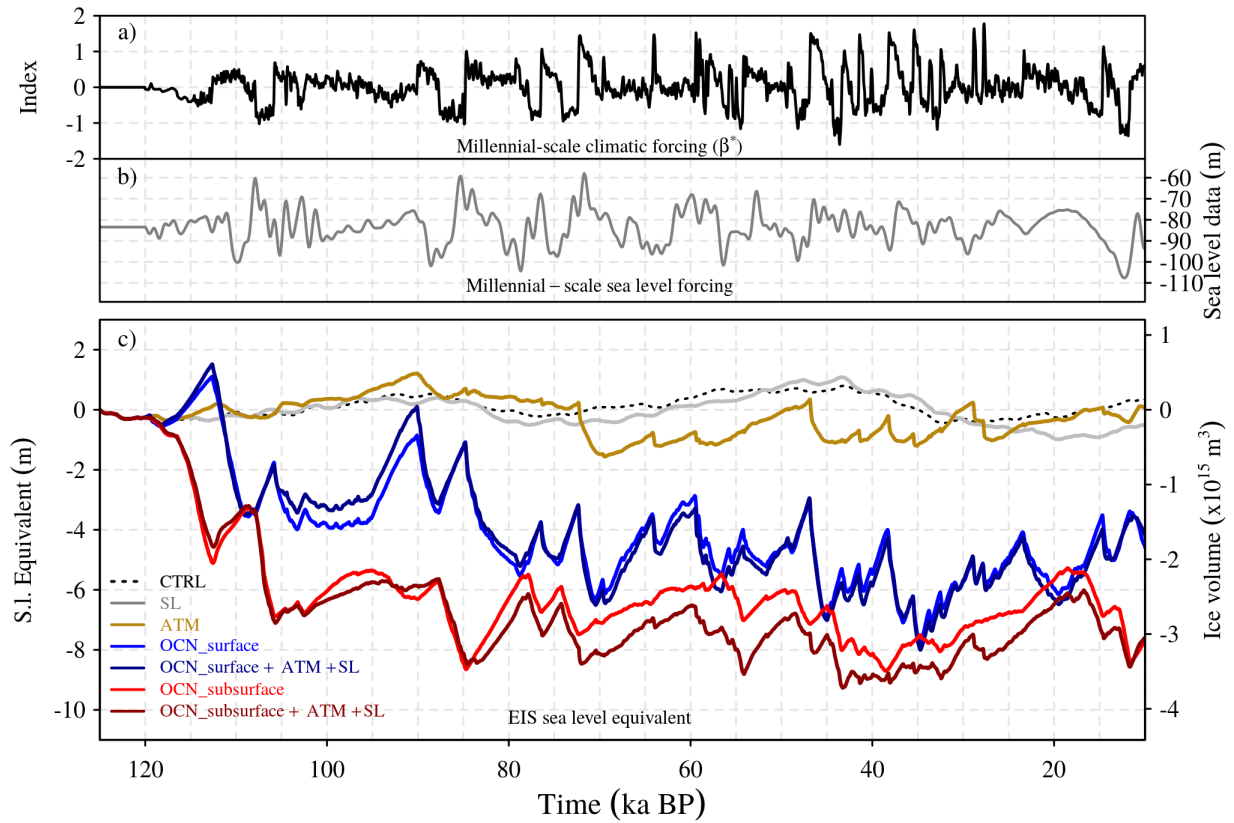


**Figure 3.** **a)** Temporal component of the millennial-scale climatic forcing ( $\beta^*$  index). **b)** Millennial-scale sea-level forcing (Grant et al., 2012). **c)** EIS sea-level equivalent (m) related to ice volume variations ( $\text{m}^3$ ) with respect to initial conditions for the CTRL (black) run and for the SL (gray), ATM (gold), OCNsrf (blue), OCNsub (red), OCNsrf + ATM + SL (dark blue), and OCNsub + ATM + SL (dark red) forcing experiments.

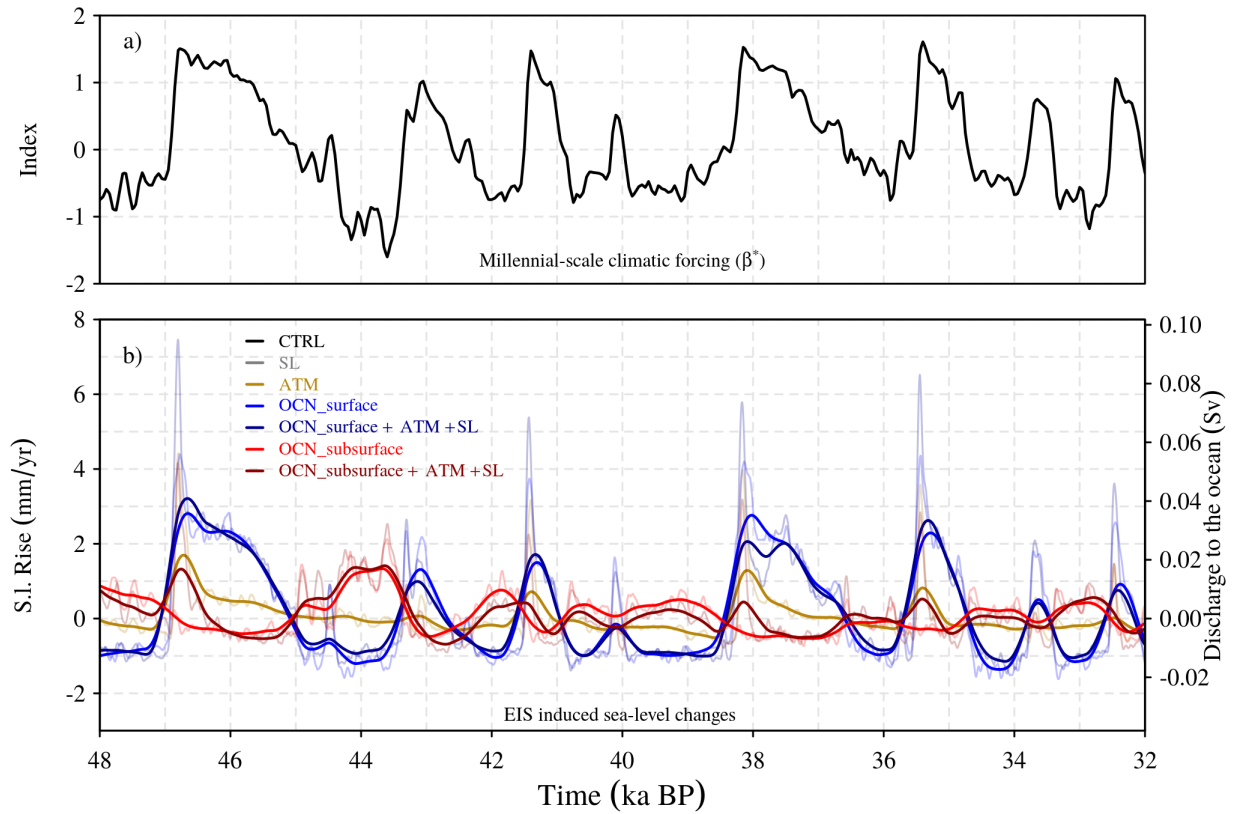


**Figure 4. Rev. 1 SC7: MIS3 Period. a)** Temporal component of the millennial-scale climatic forcing ( $\beta^*$  index), and **b)** EIS changes (mm/yr and Sv) related to ice volume variations ( $m^3$ ) with respect to initial conditions for the CTRL (black) run and for the SL (gray) ATM (gold), OCNsrf (blue), OCNsub (red), OCNsrf + ATM + SL (dark blue), and OCNsub + ATM + SL (dark red) forcing experiments.

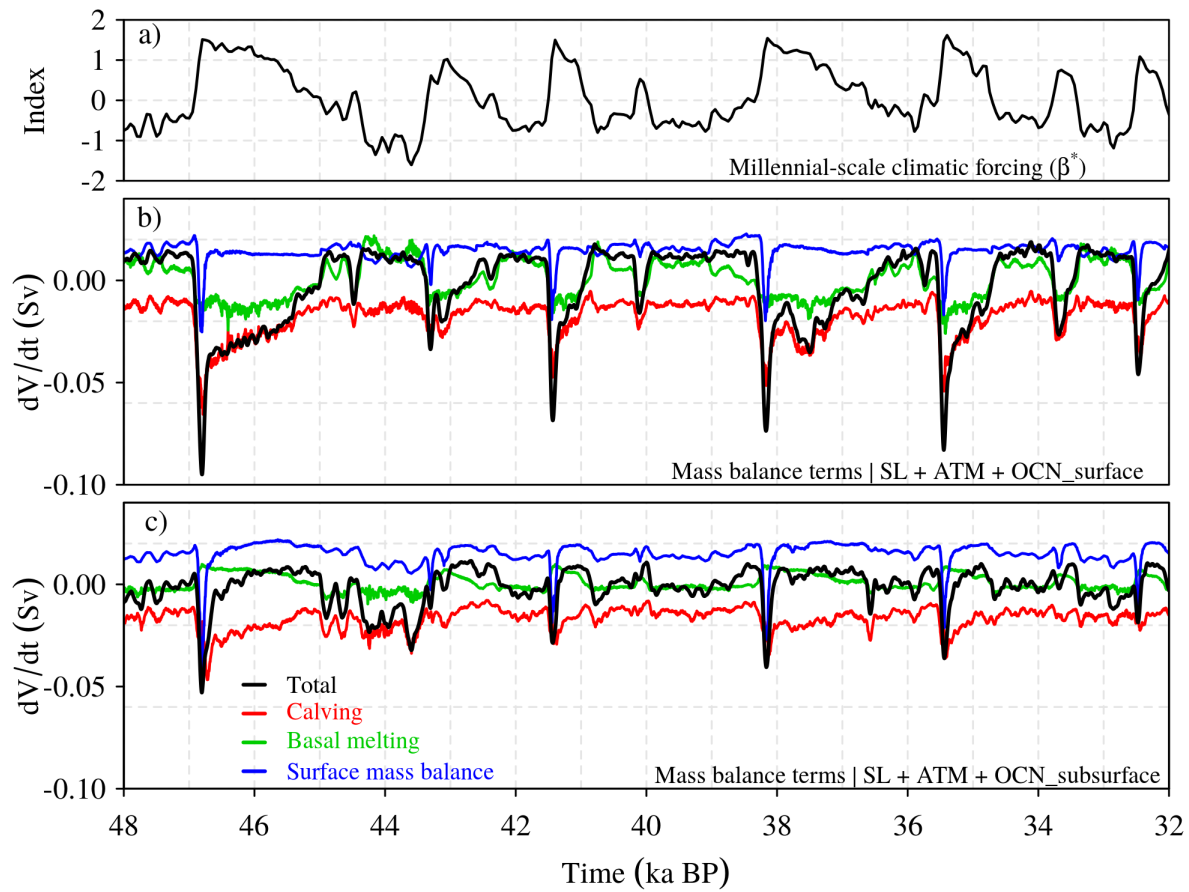


**Figure 5.** MIS3 Period. **a)** Temporal component of the millennial-scale climatic forcing ( $\beta^*$  index), and contribution of the different terms of the EIS mass balance to ice volume variations ( $m^3$ ) in simulations considering all forcings, with **b)** corresponding to the surface oceanic forcing and **c)** to the subsurface oceanic forcing.

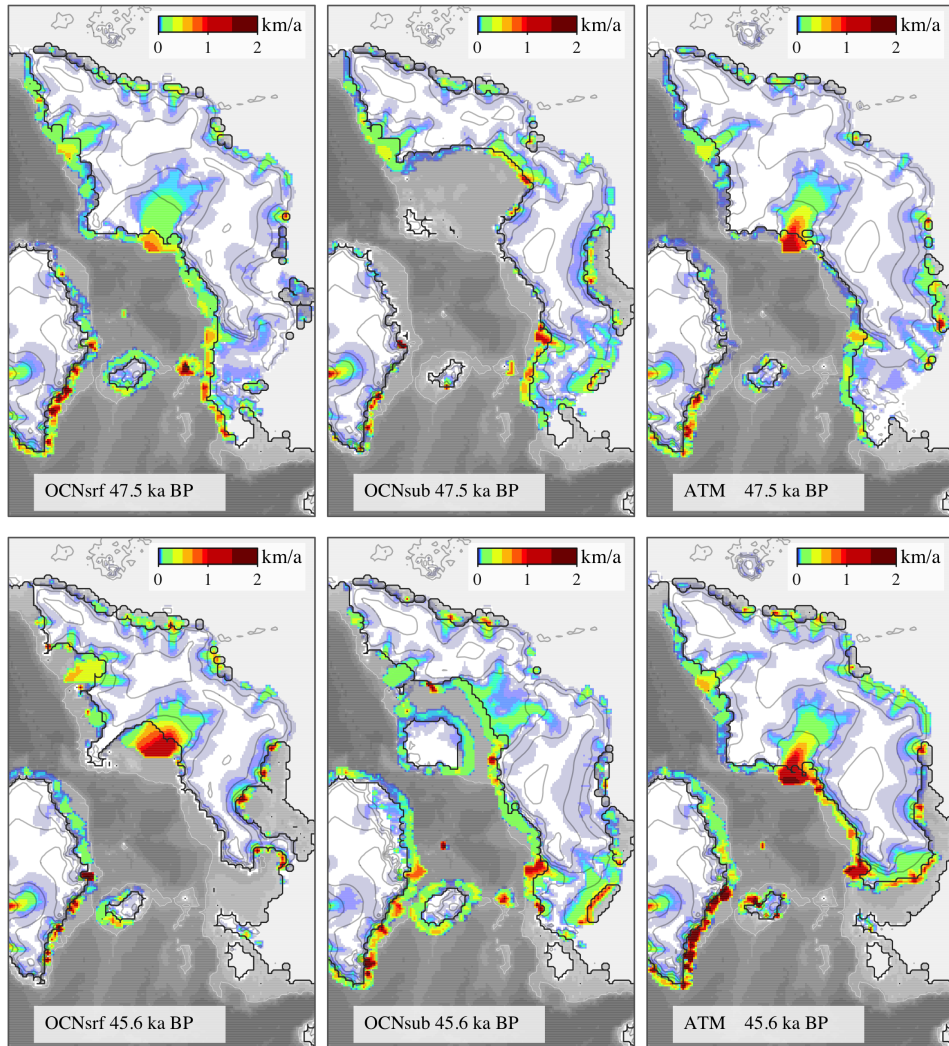


**Figure 6.** Simulated EIS at the end of a stadial period (upper panels) and at the end of an interstadial period (lower panels) for the experiments: OCNsrf (left); OCNsub (middle) and ATM (right). Shaded colors show ice velocities ( $\text{km a}^{-1}$ ). The ice thickness contours are plotted for every 500 m with the grounding line position shown by a black line. The 500 m depth contour is shown by the white line. [Rev. 2 SC 25](#) The periods represented here corresponds to the stadial and interstadial periods previous and posterior to DO 12 (ca. 47 ka BP), respectively.

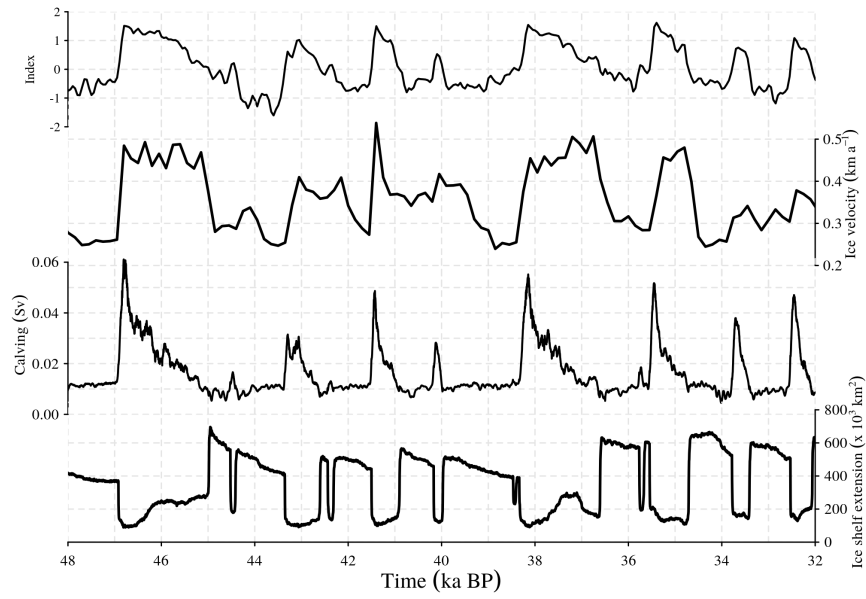


**Figure 7.** MIS3 Period. Temporal component of the millennial-scale climatic forcing ( $\beta^*$  index), ice velocities in the Bjørnøyrenn basin ( $km a^{-1}$ ), calving rate (Sv) and ice-shelf extension ( $10^3 km^2$ ) in the OCNsrf simulation.

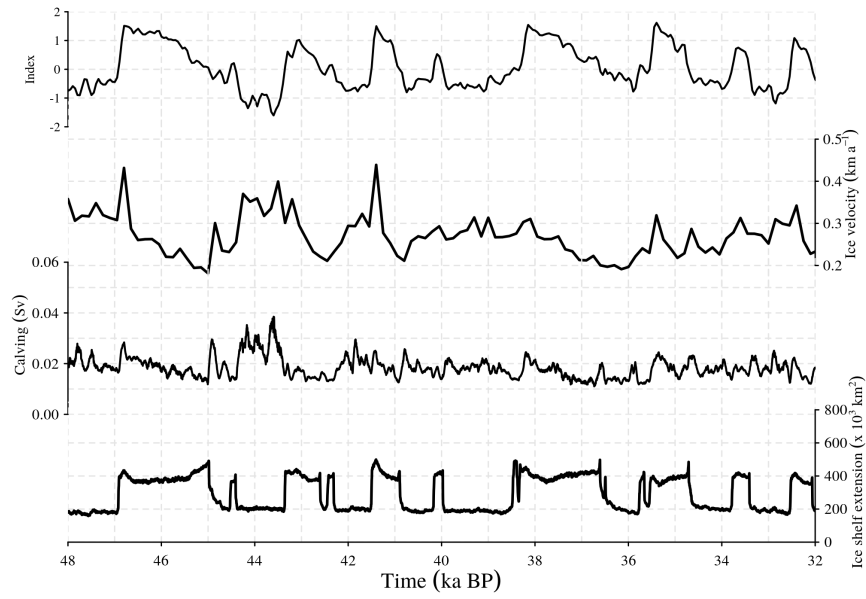


**Figure 8.** MIS3 Period. Temporal component of the millennial-scale climatic forcing ( $\beta^*$  index), ice velocities in the Bjørnøyrenn basin ( $km a^{-1}$ ), calving rate (Sv) and ice-shelf extension ( $10^3 km^2$ ) in the OCNsub simulation.

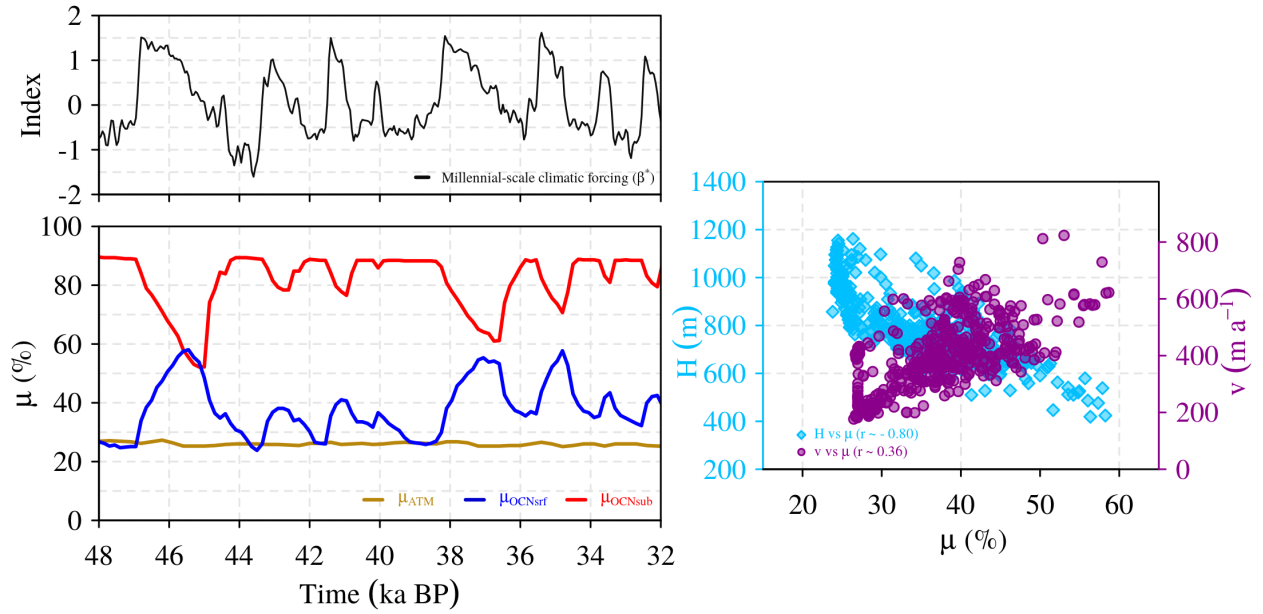


**Figure 9.** Dynamic behavior of the EIS during millennial-scale climatic transitions for the OCN and ATM experiments. **a)** Displacement of the grounding line in the Bjørnøyrenn basin in response to the climatic  $\beta^*$  forcing (gray). The evolution of the grounding line position is shown for OCNSrf (blue), OCNsub (red) and ATM (gold). The migration of the grounding line has been characterized as an index  $\mu(t)$  that represents the evolution of the number of points of grounded ice  $N_g(t)$  over a fixed area of  $N$  points in the Barents Sea region. Positive values of  $\mu$  indicate grounding line retreat. **b)** Scatter plot diagram showing the relationship between ice thickness  $H$  in the region of the Bjørnøyrenna basin and  $\mu$  (light blue diamonds;  $r(\mu, H) \simeq -0.80$ ) as well as the relationship between ice-stream velocities  $v$  in the same region and  $\mu$  (purple circles;  $r(\mu, v) \simeq 0.36$ ).

# Supplementary Information for the article: Oceanic forcing of the Eurasian Ice Sheet on millennial time scales during the Last Glacial Period

## 1. On the sensitivity to the ocean heat flux coefficient

As advanced in the main text, in order to investigate the sensitivity of the results to the model parameters, eight additional OCN simulations, both for the surface and the subsurface, have been carried out with different  $\kappa$  parameters between 1 and 9 m/yr/K, i.e., bracketing our standard case of  $\kappa = 5$  m/yr/K, both for the OCNsrf and the OCNsub cases.

This choice reflects the inferences based on measurements made on Antarctic ice shelves (Rignot and Jacobs, 2002)

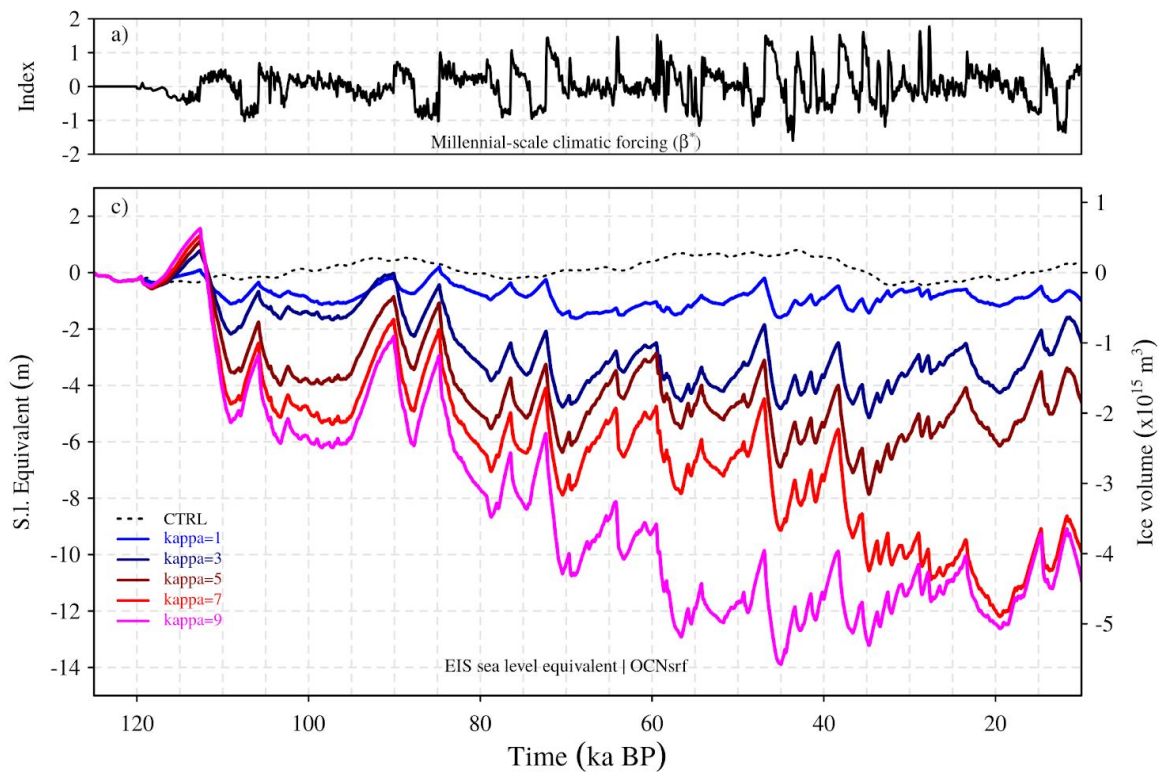


Figure S1 | Volume time series of the EIS for different values of the ocean heat flux coefficient corresponding to the OCNsrf forcing.

A robust response of the EIS is found, with a more reactive EIS response for increasing  $\kappa$  values, as shown in Figures S1 and S2.

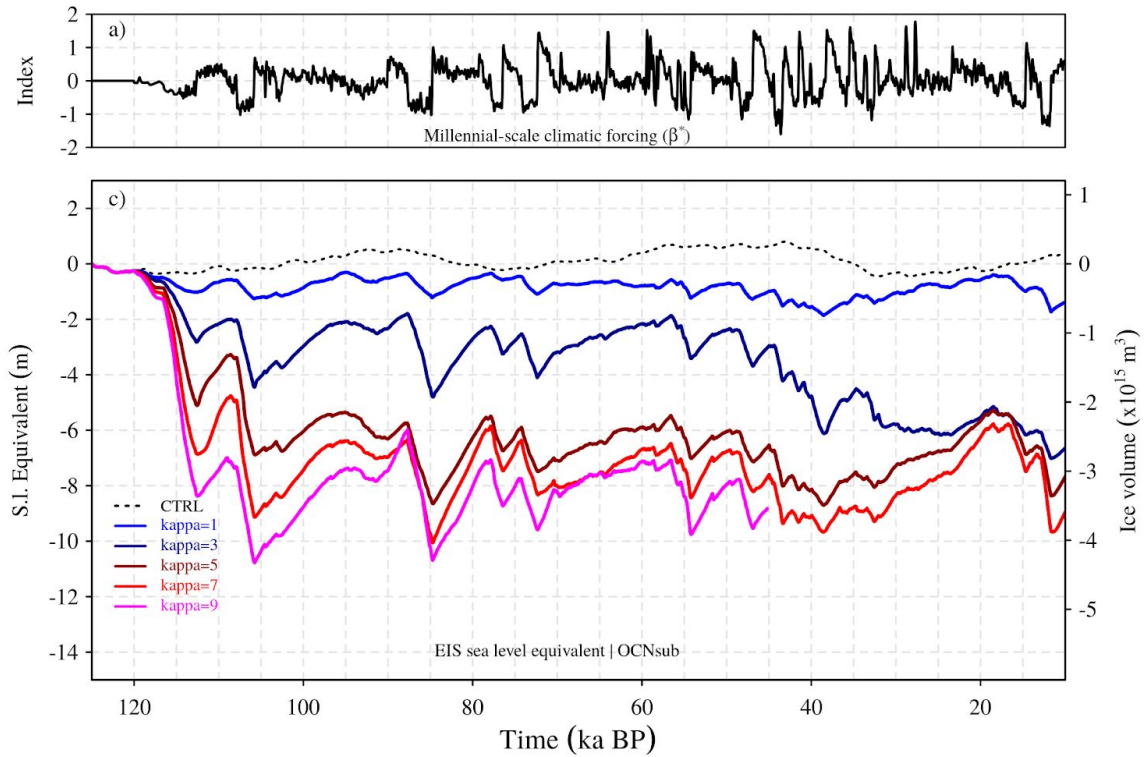


Figure S2 | Volume time series of the EIS for different values of the ocean heat flux coefficient corresponding to the OCNsub forcing.

## 2. On the sensitivity to the atmospheric forcing

To assess the uncertainty associated to the PDD approach, the potential interplay between different parameterizations of the refreezing water on the ice from surface ablation, and the response of the ice sheet to different oceanic sensitivities in terms of its dynamics, we performed new ensemble of simulations.

We first explored the uncertainty of the PDD model by changing the value of its parameters. The simulations shown in the main text correspond to the following values of the PDD model:

$\sigma = 5 \text{ K}$ ,  $f_{\text{PDD\_ice}} = 0.008 \text{ mwe/PDD}$  and  $f_{\text{PDD\_snow}} = 0.003 \text{ mwe/PDD}$

We have also explored the sensitivity of our ice sheet model to the following range of values of these parameters:

$\sigma$ : 4,5,6 K

$f_{\text{PDD\_snow}}$ : 0.0015, 0.003, 0.006 mwe/PDD

$f_{\text{PDD\_ice}}$ : 0.004, 0.008, 0.016 mwe/PDD

Therefore, the sensitivity of our results to the values of the atmospheric mass balance model has also been explored in 91 additional simulations that are illustrated in Fig S2.

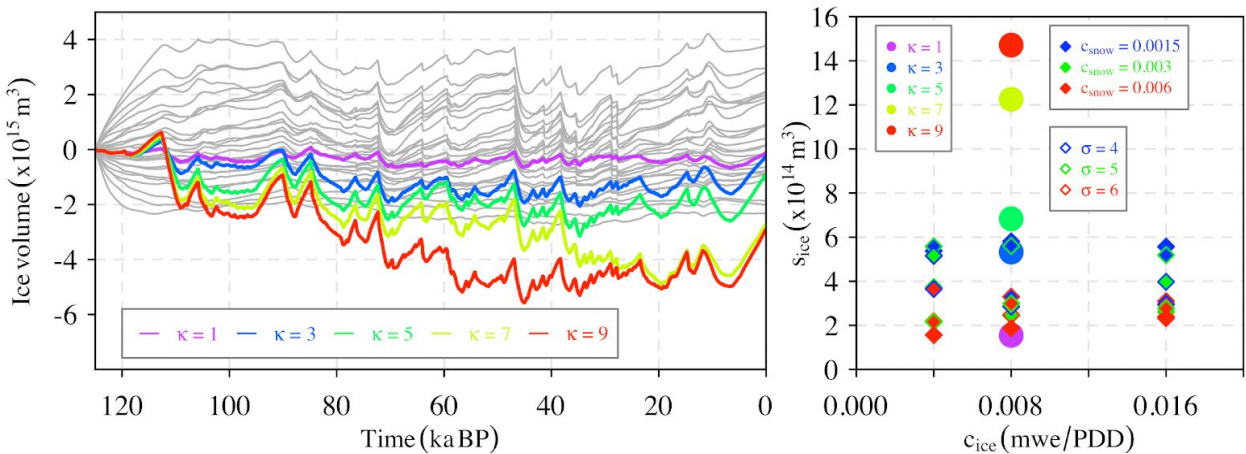


Figure S3 | Left: Time series of EIS volume. Gray trajectories represent the 91 realisations of perturbing the PDD parameters. The sensitivity shown by different values of the ocean heat flux coefficient,  $\kappa$ , is included by means of the OCNsrf time series in colors. Right: Scatter plot of the amplitude of the millennial oscillations (standard deviation of the volume time series) for the PDD ensemble (diamonds) together with the OCNsrf (circles)

Figure S3 (right panel) shows the variability of the 91 simulations exploring the uncertainty of the PDD model in terms of the standard deviation of the time series for the period 100 - 10 ky BP. This amplitude is compared with the one shown by exploring the values of  $\kappa$  (from 1 to 9 m/yr/K) in a OCNsrf ensemble. A greater amplitude when forcing with the ocean is found from  $\kappa = 3$  m/yr/K.

The potential interplay between the amount of refreezing from surface ablation and the response to an oceanic warming has also been investigated by considering different values of the refreezing parameter,  $r$ , and the sensitivity to the ocean,  $\kappa$ , (Figure S3).

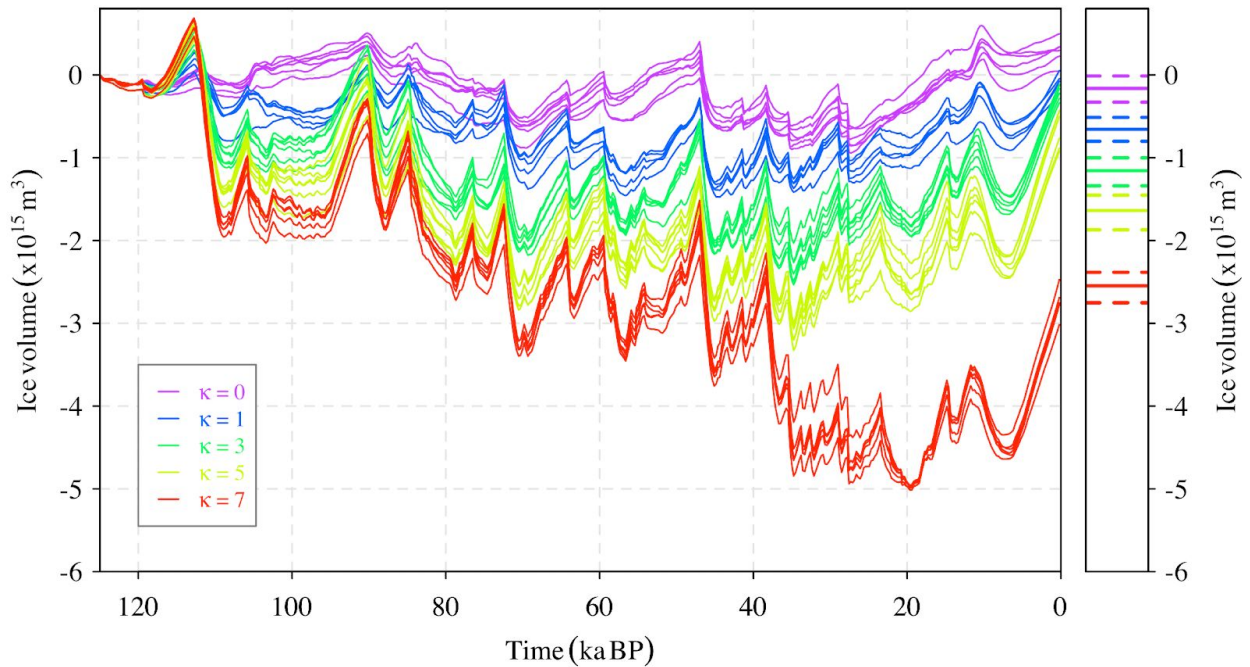


Figure S4 | EIS volume time series for different values of  $r$  (= 0.0, 20, 40, 60, 80 and 100%) per each value of  $\kappa$  (= 0, 1, 3, 5 and 7 m/yr/K).

Right panel in Figure S3 illustrates the mean values of the different realisations of the model corresponding to different values of the parameter  $r$ , for a given value of  $\kappa$ . Dashed lines represent the standard deviation of these simulations. Note that the proportion of the water produced from surface ablation that is allowed to refreeze in the ice does not directly change the viscosity in our model but the surface mass balance. Thus our ensemble is intended to illustrate the potential relationship between a larger ablation (for a given surface warming) and the dynamic response of the ice sheet to an oceanic perturbation. The analysis of this new ensemble shows a negligible amplification effect from reduced (or increased) refreezing from surface waters on the dynamic behavior of the ice sheet.